Energy 344 (2026) 140052

Contents lists available at ScienceDirect

Energy

journal homepage: www.elsevier.com/locate/energy

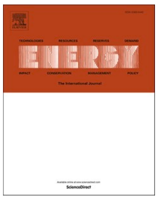

Design, performance assessment, and machine learning-driven optimization of a novel low-carbon urban waste-to-x polygeneration system: multi-scenario analysis of hydrogen and methane production

Mohammadreza Babaei Khuyinrud [a], Ali Shokri Kalan [b,*], Borhan Pourtalebi [c], Mehran Ahamdi [d], Iraj Jangi [e], Xiaoshu Lü [b,f], Yanping Yuan [g], Marc A. Rosen [h]

[a] *Faculty of Mechanical Engineering, Sahand University of Technology, Sahand New Town, P.O. Box, 51335-1996, Tabriz, Iran*
[b] *Renewable Energy and Built Environment, University of Vaasa, P.O. Box 700, FIN-65101, Vaasa, Finland*
[c] *Chemical Engineering Faculty, Sahand University of Technology, Sahand New Town, P.O. Box 51335-1996, Tabriz, Iran*
[d] *Department of Industrial Engineering, University of Padova, Via Venezia 1, Pado- va, 35131, Italy*
[e] *Faculty of Chemical and Petroleum Engineering, University of Tabriz, 29 Bahman Blvd., Tabriz, Iran*
[f] *Department of Civil Engineering, Aalto University, P.O. Box. 11000, FIN-02130, Finland*
[g] *School of Mechanical Engineering, Southwest Jiaotong University, Chengdu, 610031, China*
[h] *Faculty of Engineering and Applied Science, University of Ontario Institute of Technology, Oshawa, Ontario, L1G 0C5, Canada*

ARTICLE INFO

Keywords:
Wastewater treatment
Biomass gasification
Carbon capture and utilization
Biofuel production
Near-zero emissions
Machine learning optimization

ABSTRACT

Growing energy demand, waste accumulation, and greenhouse gas emissions necessitate integrated, low-carbon energy options. This study proposes a novel waste-to-x polygeneration system uniquely integrating biomass gasification with gas turbine, supercritical CO_2, Kalina, organic Rankine, and steam Rankine cycles, coupled with advanced wastewater treatment, carbon capture, a proton exchange membrane (PEM) electrolysis, and methanation. The system simultaneously produces electricity, district heat, oxygen, hydrogen, and methane, advancing beyond typical waste-to-energy approaches by combining multi-vector fuel production with near-zero emissions. Under baseline operation, the system attains overall energy and exergy efficiencies of 35.0 % and 39.9 %, delivering 3510 kW net power and 1310 kW heating, and daily outputs of 131.6 kg hydrogen, 2106 kg oxygen, and 296.3 kg methane, while capturing 87 % of CO_2 emissions (177.7 t/day) and treating 116.6 t/day wastewater. Exergy analysis identifies the biomass gasifier as the primary exergy destruction source (8014 kW), whereas mixers and splitters achieve the highest exergy efficiencies (>99.0 %). Employing a machine-learning-assisted multi-objective grey wolf optimizer (MOGWO), for dual fuel production scenario, enhances energy and exergy efficiencies to 49.5 % and 53.6 %, respectively; boosts hydrogen, oxygen, and methane production by 23.0 %; reduces net power by 6.9 %; and increases heating output by up to 29.1 %. Among fuel-production modes at the optimum, the hydrogen-only case achieves the highest efficiencies (49.7 % energy, 53.6 % exergy). This integrated approach offers a comprehensive and flexible option for sustainable urban resource management.

Nomenclature		PR	Pressure ratio
ABS	Absorber	$\dot{Q}$	Heat transfer rate (kW)
AC	Air compressor	$\bar{R}$	Universal gas constant (kJ/kmol.K)
AF	Air–fuel ratio	RC	Re-compressor
ANN	Artificial neural network	Ru	Ruthenium
APH	Air pre-heater	s	Specific entropy (kJ/kg.K)
BECCS	Bioenergy with carbon capture and storage	s-CO_2	Supercritical carbon dioxide
CC	Combustion chamber	SEP	Separator
CCU	Carbon capture and utilization	SM	Sabatier methanation
CD	Condenser	SPL	Splitter
CH_4	Methane	SR	Split ratio

(*continued on next page*)

---

* Corresponding author.
E-mail address: Ali.Shokrikalan@uwasa.fi (A. Shokri Kalan).

https://doi.org/10.1016/j.energy.2026.140052
Received 18 October 2025; Received in revised form 9 December 2025; Accepted 13 January 2026

(*continued*)

CHP	Combined heat and power	SRC	Steam Rankine cycle
COMP	Compressor	T	Temperature (K)
CO	Carbon monoxide	TEG	Thermoelectric generator
CO_2	Carbon dioxide	THV	Throttle valve
DGY	Dry gas yield	V	Cell potential (V)
DWH	District water heating	$\dot{W}$	Electrical power (kW)
E	Exergy rate (kW)	WtE	Waste-to-Energy
EVA	Evaporator	X	Mole fraction
$\bar{g}$	Molar Gibbs free energy (kJ/kmol)	ZT	Figure of merit
GEN	Generator	**Greek symbols**	
GT	Gas turbine	β	Coefficient for chemical exergy of biomass
h	Specific enthalpy (kJ/kg)	**Δ**	Difference
H_2	Hydrogen	η_I	Energy efficiency (%)
H_2O	Water	η_{II}	Exergy efficiency (%)
HEX	Heat exchanger	ε	Effectiveness (%)
HTR	High-temperature recuperator	λ	Water content
J	Current density (A/m^2)	σ(x)	Local ionic conductivity of PEME membrane (S/m)
K	Equilibrium constant of reaction	**Subscripts**	
KC	Kalina cycle	0	Dead state, at ambient T and P
LHV	Lower heating value (kJ/kg)	an	Anode
LTR	Low-temperature recuperator	ca	Cathode
$\dot{m}$	Mass-flow rate (kg/s)	ch	Chemical
MC	Moisture content	D	Destruction
MEA	Monoethanolamine	e	Outlet
MIX	Mixer	F	Fuel exergy
MOGWO	Multi-objective grey wolf optimizer	H	High
MSW	Municipal solid waste	i	Inlet
MW	Molecular weight (kg/kmol)	is	Isentropic
NH_3	Ammonia	k	kth component
N_2	Nitrogen	L	Low
ORC	Organic Rankine cycle	min	Minimum
P	Pressure (kPa)	P	Product exergy
PCCC	Post-combustion carbon capture	ph	Physical
PEME	Proton exchange membrane electrolyzer	sab	Sabatier process

1. Introduction

In recent years, the growing global population and industrialization have led to a substantial rise in energy requirements, increasing dependence on fossil fuels and further intensifying greenhouse gas emissions and global warming [1,2]. To confront these issues, the Paris Agreement established an ambitious target of reaching carbon neutrality by the year 2050 [3]. Transitioning to renewable energy sources is considered an essential strategy for meeting this target [4]. Among renewable energy sources, municipal solid waste (MSW), as a type of biomass, presents a valuable opportunity for urban power generation. Utilizing MSW not only satisfies energy demands but also mitigates environmental pollution by reducing landfill volumes [5]. Additionally, integrating CO_2 capture technologies during MSW utilization is crucial to accelerating progress toward the carbon-free environment [6]. Yet, owing to the inconsistency in renewable energy supply, incorporating energy storage systems is essential for ensuring system reliability. Hydrogen production through electrolysis, along with the synthesis of alternative fuels like biomethane, can provide effective long-term storage options to address the challenges of energy intermittency [7]. Furthermore, in urban wastewater treatment, the reuse of water plays a vital role in shifting the sector towards a circular economy [8]. The utilization of waste heat from thermal processes presents a viable strategy for freshwater generation. Concurrently, the global energy landscape is undergoing a significant transformation. This transition is propelled by the increasing adoption of renewable energy sources, in tandem with progress in hydrogen production, carbon capture technologies, and the synthesis of value-added bio-products like methane. These developments are essential for advancing sustainability and achieving effective decarbonization.

Biomass is categorized into six principal classifications, with municipal solid waste (MSW) and municipal wastewater holding particular significance for urban environments [9]. The utilization of MSW as a feedstock for Waste-to-Energy (WtE) systems serves a dual function, facilitating both waste management strategies and renewable electricity production, owing to the widespread availability of these resources [10]. Furthermore, WtE systems demonstrate carbon neutrality, generate substantial employment prospects, and play a crucial role in climate change mitigation efforts [11]. There are several WtE methods, including combustion, pyrolysis, and anaerobic digestion [12]. However, gasification stands out because of its multiple advantages. It can process various types of biomass materials, such as (MSW), industrial waste, and other forms of biomass [13]. In addition, gasification produces a cleaner gas than combustion and pyrolysis, boasts higher energy recovery efficiency, and has better heat capacity performance [14]. In addition, applying combined heating and power (CHP) driven by biomass could boost the efficiency of the system, while reducing carbon emissions [15]. Numerous thermodynamic cycles, such as the Brayton cycle [16], Organic Rankine cycle (ORC) [17], Stirling engine cycle [18], supercritical CO_2 (s-CO_2) cycle [19], and Kalina cycle [20], have been developed and investigated for their potential to recover waste heat across a range of temperature levels [21]. The integration of supercritical CO_2, Kalina, and other advanced cycles provides unique benefits, such as higher heat recovery efficiency and better system performance. The synergies between these cycles, which operate at different temperature levels, allow for optimized energy use, making the system more efficient and flexible than traditional waste-to-energy systems. This integrated approach, alongside biomass gasification and advanced optimization, enables the simultaneous production of electricity, heat, hydrogen, methane, and oxygen, offering a comprehensive, environmentally friendly option [22].

Kalan et al. [23] developed a trigeneration system powered by municipal solid waste gasification, combining a modified Kalina cycle with a supercritical CO_2 cycle to simultaneously produce cold, heat, and electricity. They achieved energy and exergy efficiencies of 71.5 % and 55.4 %, respectively. Xiao and Wu [24] focused on developing an MSW gasification-based multi-generation system that combines a solid oxide fuel cell (SOFC), heat recovery unit, and fluidized bed gasifier. Their research demonstrated that optimized conditions improved system efficiencies and reduced emissions. Biancini et al. [25] investigated integrating gasification of residual MSW within composting facilities. The gasification process produces bio-crude oil at annual rates between 9617 and 12718 tonnes and contributes to electricity production of up to 5185 kW, demonstrating significant potential for energy recovery.

The utilization of biomass as a principal energy source can contribute to the attainment of carbon neutrality. However, the integration of bioenergy systems with carbon capture and storage (BECCS) technologies facilitates the realization of net-negative emissions, thereby expediting the accomplishment of environmental objectives [26]. Carbon capture and storage (CCS) technologies are broadly categorized into three principal types: post-combustion, pre-combustion, and oxy-fuel combustion capture [27]. Among these, post-combustion carbon capture (PCCC) stands out for its advanced level of development, minimal modifications required for existing combustion setups and equipment, reduced investment costs, and simpler maintenance and operational demands [28]. There are various approaches to PCCC, but four primary techniques are widely adopted in practice: solvent-based absorption, solid sorbent adsorption, membrane separation, and cryogenic processes [29]. Among these methods, solvent-based absorption is the most established and widely utilized approach. Monoethanolamine (MEA) remains the most commonly used amine solvent for CO_2 removal due to its affordability, fast reaction kinetics, and high mass transfer rates [30].

Dong et al. [31] evaluates the potential for CO2 capture within Sweden's biomass and waste-fired combined heat and power (CHP) plants, finding that operating mode 1 (OM1) can achieve up to 8.7 million tons of negative emissions annually. Based on a levelized cost assessment, the CO_2 avoidance costs are determined to be 37 USD per ton for OM1 and 52 USD per ton for OM2, with the biogenic fraction of the waste exerting a significant influence on these costs. Zhu et al. [32] proposed a novel biomass-fired CCHP system combining ORC, lithium bromide absorption refrigeration, and MEA-based CO_2 capture. Their study found optimal operation parameters that achieve high thermal efficiency (81.5 %), refrigeration efficiency (14 %), and primary energy saving ratio (13.3 %), while also enabling negative CO_2 emissions due to integrated carbon capture. Beiron et al. [33] analyzed the potential for CCS in Sweden's 110 biomass- or waste-fired CHP plants. Based on the process and system simulations, the achievable CO_2 capture capacity is estimated to be around 19.3 $MtCO_2$ per year, with costs ranging from 45 to 125 €/tCO_2, which supports Sweden's proposed BECCS targets of 3–10 Mt annually by 2045.

Hydrogen has gained significant attention as a carbon-free energy carrier with high energy density (on a mass basis) and broad applicability in power generation, transportation, and industry [34]. There are various methods for hydrogen production, with the majority currently being derived from fossil fuels. However, one way of producing hydrogen for which interest is growing is water electrolysis. Among the various electrolysis technologies, proton exchange membrane (PEM) electrolyzers are distinguished by their high current density, compact configuration, and capability to generate hydrogen at elevated pressures. They also exhibit rapid dynamic response, strong performance under variable power input, and excellent compatibility with intermittent renewable energy sources [35]. However, the storage of hydrogen poses significant challenges, particularly when large volumes are required [36]. To address these challenges, carbon capture and utilization (CCU) has emerged as a potential approach for producing alternative energy carriers [37]. Catalytic hydrogenation of CO_2 with renewable hydrogen is viewed as a potential pathway for sustainably producing lower olefins, higher hydrocarbons, methanol, formic acid, and higher alcohols [38]. Among the various synthetic fuels derived from CCU, methane (CH_4) is particularly attractive due to the widespread availability of an extensive distribution network and well-established regulatory frameworks [39].

Jalili et al. [40] compared two power-to-methane systems: one with a PEM electrolyzer and Sabatier reactor, and another with a solid oxide electrolyzer and methanation reactor. The PEM-based setup showed higher productivity, while the SOEC-based system produced 1.2 % more methane and a 7.6 % higher lower heating value. Sabaghi et al. [41] developed a biomass-powered multi-generation system integrating s-CO_2 and t-CO_2 cycles, a modified gas turbine, PEM electrolyzer, and fuel cell. Using various biomass types, including MSW, the system achieved 47.9 % energy and 32.3 % exergy efficiency, producing 2.7 kg/h of hydrogen, with MSW yielding the highest performance. García-Luna et al. [42] examined advanced WtE plant designs with 30 % MEA CO_2 capture and CH_4 conversion, comparing conventional Waste-to-Gas with Partial OxyWaste-to-Gas (featuring integrated PEM electrolyzers). The Partial OxyWaste-to-Gas scenario demonstrated lower methane costs (100–138 €/MWh) and reduced energy penalties (1.5 %).

As mentioned earlier, in urban areas, wastewater treatment is one of the most significant challenges. This issue can be addressed by coupling such a system with biomass-fuelled energy systems and utilizing the waste heat for water purification, ultimately contributing to cleaner environments. In this regard, Schyllander et al. [43] studied an industrial symbiotic system in Karlstad, Sweden, integrating algal cultivation, a CHP plant, and wastewater treatment. Wastewater digestate from the anaerobic digester provided nitrogen and phosphorus, while waste heat and exhaust gases supported algae drying and CO_2 supply. The system boosted algal productivity from 14 to 18 g/m^2/day and achieved net energy ratios of 2.6–5.3. Gupta and Khatiwada [44] assessed waste-to-energy recovery in a wastewater treatment plant in Tbilisi, Georgia, for 2018 to 2040. They found that combined wastewater and sewage sludge recovery could generate 137 GWh/year and avoid 38,500 tCO_2eq emissions, with financial feasibility shown by an NPV of 14.9 million EUR and a levelized biogas cost of 0.08 EUR/m^3.

Although notable developments have occurred in the advancement of waste-to-energy technologies, many studies still provide only a partial response to the combined challenges of environmental sustainability, net-zero emissions, and integrated urban resource management. Urban areas face unique constraints in simultaneously managing municipal solid waste, wastewater, and greenhouse gas emissions, yet most existing WtE concepts focus on either electricity/heat generation or single-environmental aspects in isolation. Prior works commonly enhance the energy efficiency of MSW-based WtE plants but rarely incorporate systematic carbon capture and storage (CCS), and when hydrogen production is included, the long-term storage and valorization of hydrogen are often not fully addressed. Only a limited number of studies consider carbon capture and utilization (CCU) to transform captured CO_2 and hydrogen into synthetic fuels, and even fewer integrate advanced waste-heat recovery, wastewater treatment, and detailed optimization into a unified, city-scale option. Furthermore, while optimization and control methods are widely used, comprehensive parametric sensitivity analyses combined with robust machine-learning-based multi-objective optimization frameworks are rarely implemented to guide design trade-offs under realistic operating conditions.

In this context, the present study advances the state-of-the-art by proposing a novel, fully integrated, urban waste-to-x polygeneration system that simultaneously: (i) treats municipal solid waste and wastewater, (ii) incorporates monoethanolamine-based post-combustion CO_2 capture to approach near net-zero emissions, and (iii) co-produces electricity, heat, hydrogen, and methane within a single architecture. The configuration couples MSW gasification with gas turbine, supercritical CO_2, organic and steam Rankine cycles, advanced wastewater treatment, PEM electrolysis, and methanation, while exploiting comprehensive waste-heat recovery (including low-grade streams via TEGs) to supply both electricity and freshwater for electrolysis. Beyond conventional WtE schemes, the proposed system closes the carbon loop by converting a portion of the captured CO_2 and generated H_2 into storable methane, directly addressing renewable intermittency and hydrogen storage constraints. The originality of this work also lies in its integrated performance assessment and decision support: the plant is evaluated through detailed energy and exergy analyses and then optimized using a machine-learning-assisted multi-objective grey wolf algorithm, enabling the simultaneous maximization of efficiency, emissions reduction, and overall sustainability and thereby providing a new benchmark for low-carbon urban polygeneration systems.

The main contributions of this work follow:

- Development of a novel, efficient polygeneration system that converts municipal solid waste and wastewater into valuable energy products with near-zero emissions.
- Integration of MEA-based carbon capture with CO_2 utilization and partial storage to mitigate emissions.
- Utilization of waste heat to produce hydrogen and methane, enhancing system sustainability, reliability and flexibility.
- Application of machine learning for comprehensive sensitivity analysis and multi-objective optimization to identify key parameters and enhance system performance.

2. System description

Fig. 1a and b illustrate the layout of the proposed innovative waste-to-x polygeneration system. The system integrates multiple subsystems, including biomass gasification, a gas turbine cycle, the Kalina cycle, a supercritical CO_2 (s-CO_2) cycle, steam and organic Rankine cycles (SRC and ORC), wastewater treatment, a proton exchange membrane electrolyzer, carbon capture and utilization, as well as a methanation unit.

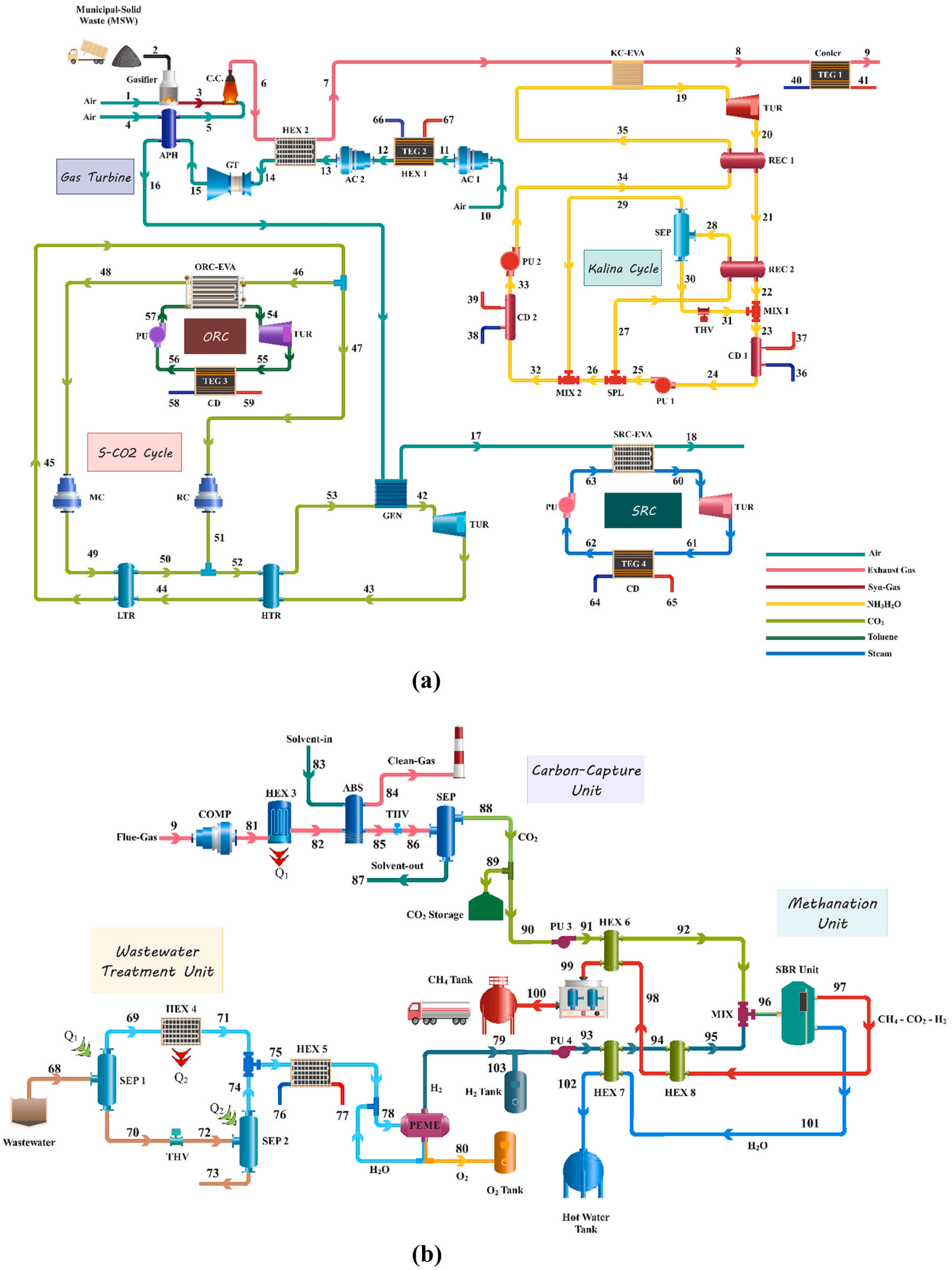

Fig. 1. Schematic of the proposed polygeneration system: **a)** Power cycles **b)** CCUS, Wastewater treatment, and Methanation.

2.1. Biomass gasification process

Fig. 1a illustrates the biomass gasification process, where municipal solid waste (MSW) with specified constituents (state 2) is first blended with air (state 1) and then introduced into the gasifier to initiate the gasification process. The generated synthesis gas (syngas, state 3) is mixed with preheated air (state 5) and directed to the combustion chamber (CC) to ensure complete combustion. The generated flue gases (state 6) are first used to transfer heat to the gas turbine cycle via Heat Exchanger 2 (HEX2). Upon leaving this unit (state 7), the exhaust stream is employed as the primary heat source for the Kalina cycle through the evaporator (KC-EVA). After delivering thermal energy to the Kalina subsystem, the cooled stream (state 8) is passed through a cooler, where it simultaneously is used to provide domestic hot water and to supply thermal energy to a thermoelectric generator (TEG1), thereby producing additional electrical power. Finally, the exhaust is conducted to the carbon capture unit for further treatment and emission reduction.

2.2. *Gas turbine cycle*

As illustrated in Fig. 1a, ambient air is first drawn into Air Compressor 1 (AC1), where its pressure is increased (state 10). The compressed air is then cooled to reduce its temperature before being further pressurized in AC2. During this process, heat is recovered in HEX1 to supply domestic hot water, while part of this thermal energy is simultaneously converted into electricity by TEG2. After recompression, the high-pressure air (state 13) is preheated using exhaust gases in HEX2. The resulting high-pressure, high-temperature stream (state 14) is expanded in the gas turbine (GT), producing mechanical power. The turbine exhaust (state 15) is used to preheat the combustion chamber (CC) inlet air. Subsequently, the outlet stream (state 16) is employed to supply thermal energy to the s-CO_2 cycle via the generator (GEN). Finally, the flow is directed to the SRC through its evaporator (state 17) before being released into the atmosphere (state 18).

2.3. *Kalina cycle*

As illustrated in Fig. 1a, the superheated ammonia–water mixture (state 19) first enters the turbine and then passes through Recuperator 1 (REC1, state 20) and Recuperator 2 (REC2, state 21), where it transfers heat to colder streams. The stream leaving REC2 (state 22) is mixed with the ammonia-lean liquid (state 31) in Mixer 1 (MIX1), producing stream 23. This stream is cooled in Condenser 1 (CD1) using water (states 36–37) and subsequently pressurized in Pump 1 (PU1). The pressurized flow splits into two branches: one branch (stream 27) is preheated in REC2 (state 28) and directed to the Separator (SEP), where it is divided into an ammonia-lean liquid (state 30) and an ammonia-rich vapor (state 29). The other branch (stream 26) combines with the vapor (state 29) in MIX2, forming the working solution (state 32). This mixture is cooled in CD2 by water (states 38–39), pressurized in Pump 2 (PU2, state 34), preheated in REC1 (state 35), and eventually superheated in the KC-EVA, completing the cycle.

2.4. *Supercritical CO_2 subsystem*

Fig. 1a illustrates the supercritical CO_2 subsystem. The working fluid (state 53) first enters GEN, where it is heated to form a high-temperature stream (state 42). This stream drives the turbine to produce mechanical power. The turbine exhaust (state 43) then flows sequentially through the high-temperature recuperator (HTR) and the low-temperature recuperator (LTR) to enable preheating, after which it is divided into two separate streams. The first stream (state 46) is used to supply heat to the ORC evaporator (ORC-EVA), then is directed into the main compressor (MC, state 48) for pressurization and is reheated in the LTR (state 49). The second stream (state 47) is sent to the re-compressor (RC), where it is pressurized (state 51), then is mixed with the flow from the LTR (state 50) before being fed into the HTR as the cold stream (state 52).

2.5. *Organic Rankine Cycle (ORC) subsystem*

As depicted in Fig. 1a, toluene is used as the working fluid. Stream 57 initially passes through the ORC evaporator (ORC-EVA), where it is heated and vaporized. The resulting vapor subsequently expands within the turbine (state 54), generating electrical power. The outlet stream (state 55) then is sent to the condenser (state 56), where heat is rejected to the cooling water. During this process, part of the released heat is recovered by TEG3 to produce additional electricity. The condensed process fluid is ultimately returned to the evaporator by a pump, thereby completing the closed-loop cycle.

2.6. *Steam Rankine Cycle (SRC) subsystem*

In the SRC subsystem (Fig. 1a), stream 63 is supplied to the evaporator, where it is converted into high-pressure steam that drives the turbine (state 60) for power production. The steam exiting the turbine (state 61) enters the condenser (state 62), where it transfers heat to the cooling water and simultaneously supplies thermal energy to TEG4 (states 64–65). The liquefied working fluid is then pressurized in the pump and is returned to the ORC-EVA, ensuring continuous operation of the cycle.

2.7. *Carbon capture unit*

As shown in Fig. 1b, the low-pressure gas stream (state 9) is first compressed in the compressor (COMP) and then is cooled in HEX3 to reach conditions suitable for CO_2 absorption (state 81). The cooled gas (state 82) is fed into the absorption column (ABS), where it flows upward in counter-current contact with the MEA solution (state 83). At the top of the ABS, the clean gas is separated and is released to the stack, while the CO_2-rich MEA solution (state 85) is withdrawn from the bottom for regeneration. The rich solvent is sent to the flash vessel (THV) for CO_2 removal (state 86). CO_2 is liberated and is collected as stream 88, while the regenerated MEA solution (state 87) exits the system for further treatment or disposal.

2.8. *Wastewater treatment unit and PEM electrolyzer*

As shown in Fig. 1b, contaminated water (state 68) is first fed into a separation vessel, where it is heated using heat from HEX3 (Q_1) and partially is evaporated to produce steam (state 69) free of dissolved salts and impurities. This purified steam is then directed to HEX4, where it is cooled and is condensed into clean water (state 71). The remaining unevaporated wastewater (state 70) is passed through a pressure-reducing valve (state 72) into a second vessel. Here, it is heated by the heat released from HEX4 (Q_2), producing additional contaminant-free steam (state 74), while the residual liquid (state 73) is separated as concentrated waste. The condensed steam from this stage is mixed with the previous flow that is converted into the total purified water output (state 75), which is suitable for industrial or potable use. The purified water is then cooled to 80 °C in HEX-5 (state 78) and is supplied to the PEM electrolyzer, generating hydrogen (state 79) and a mixed stream of oxygen and water. The water from this mixture is recycled to the PEM electrolyzer, while the oxygen is collected and is stored in tanks (state 80).

2.9. *Methanation unit*

As shown in Fig. 1b, the captured CO_2 stream is first pressurized by PU3 (state 91) and is preheated in HEX6 before being fed to the mixer (state 92). Simultaneously, hydrogen from the PEM electrolyzer is pressurized by PU4 (state 93) and is sequentially heated in HEX7 and HEX8 before being directed into the same mixer (state 95). The resulting CO_2–H_2 mixture is introduced into the reactor (state 96), where the methanation reaction is carried out. Throughout the reaction, the produced steam is extracted from the mixture by means of a vapor-permeable selective membrane and subsequently discharged from the system. The residual heat from the reactor off-gas is utilized to preheat the inlet streams. Subsequently, the methane produced via synthesis (state 99) undergoes temperature reduction and pressurization through a compressor equipped with an intercooler, preparing it for storage under controlled conditions (state 100).

3. Methodology

The thermodynamic model of the proposed system was developed using the operating and design parameters listed in Table 1. The complete system was simulated in Engineering Equation Solver (EES), with thermodynamic properties sourced from its library. For the wastewater treatment and CO_2 capture sub-processes, Aspen HYSYS was utilized, employing the Peng-Robinson and ACID GAS property packages, respectively. Finally, a machine learning approach in MATLAB was used to perform the optimization.

3.1. Mathematical modeling of the proposed system

Thermodynamic modeling is applied to the individual subsystems under the assumption of steady-state operation, which is a common and reasonable approach for evaluating the overall system performance under stable conditions. Although some components may exhibit dynamic behavior in practice, their short-term fluctuations are negligible compared to the system's long-term operation, making the steady-state assumption appropriate for this analysis. The other modeling assumptions are as follows:

a) The condenser's cooling water inlet temperature is set to 20 °C [53].
b) Kinetic and potential energies are considered negligible [53].
c) All condenser outlet streams are considered to be in a saturated liquid state, while the inlet stream of the ORC turbine is assumed to be saturated vapor [53].

The mathematical model of the proposed system is developed based on the fundamental laws of mass and energy conservation. In this work, the general mass and energy balance relations, formulated according to the standard expressions provided in Ref. [54], are applied at the component level throughout the system. Assuming negligible changes in kinetic and potential energies, the specific physical exergy is calculated as follows [54]:

$$e_{ph} = (h - h_0) - T_0(s - s_0) \tag{1}$$

For a mixture of ideal gases, the specific molar chemical exergy is given as [55]:

$$\bar{e}^{CH}_{Mixture} = \sum_{i}^{\sum_i} X_i \bar{e}_i^{CH} + \bar{R}T_0 \sum_{i}^{\sum} X_i \, ln \tag{2}$$

Here, X_i and $\bar{e}_i^{CH}$ denote the mole fraction and the standard chemical exergy of each component in the mixture, respectively. As a consequence of the changing ammonia concentration in the Kalina cycle, it is important to account for the corresponding variations in specific chemical exergy, expressible as [55]:

$$e_{ch} = \left[\frac{\bar{e}^0_{ch,NH_3}}{M_{NH_3}}\right] x + \left[\frac{\bar{e}^0_{ch,H_2O}}{M_{H_2O}}\right](1 - x) \tag{3}$$

where $\bar{e}^0_{ch,NH_3}$, $\bar{e}^0_{ch,\ H_2O}$, M_{NH_3} , and M_{H_2O} denote the standard molar chemical exergies of ammonia and water, along with their respective molar masses. The overall exergy rate at each state is evaluated using the following expression [55]:

$$\dot{E}_{tot} = \dot{E}_{PH} + \dot{E}_{CH} \tag{4}$$

3.1.1. Gasifier

The general equation representing the chemical reactions occurring during the gasification process can be given as follows [45]:

$$(CH_xO_y + wH_2O) + m(0.21O_2 + 0.79N_2) \rightarrow a_1H_2 + a_2CO + a_3CO_2 + a_4H_2O + a_5CH_4 + a_6N_2 \tag{5}$$

Table 1
System thermodynamic modeling parameters for operation and design.

Parameter	Value	Unit	Reference
Reference temperature	293.15	K	–
Reference pressure	1.013	bar	–
Biomass gasification			
MSW LHV	13980	kJ/kg	[45]
Biomass mass flow rate	1.155	kg/s	[45]
The heat of formation	−221579	kJ/kmol	[45]
Temperature of the syngas	823.15	K	[45]
Mass flow rate of syngas	3.683	kg/s	[45]
Moisture content	14.93	(wt. %)	[45]
MSW chemical composition	$CH_{1.46}O_{0.69}$	–	[45]
Molar equivalence ratio	0.7	–	[45]
Oxygen mole fraction in air	21	%	[45]
Nitrogen mole fraction in air	79	%	[45]
Gas turbine cycle			
$dP_{Hot,APH}$	1.5	%	[46]
$dP_{Cold,APH}$	3	%	[46]
$\eta_{is,AC1}$	87	%	[46]
$\eta_{is,AC2}$	87	%	[46]
$\eta_{is,GT}$	89	%	[46]
T_{12}	280	K	[46]
PR_{AC1}	2.3	–	[46]
PR_{AC2}	2.3	–	[46]
T_{14}	1500	K	[46]
Supercritical CO_2 cycle			
PR_{MC}	3.09	–	[23]
PR_{RC}	2.968	–	[23]
T_{max}	823.15	K	[23]
$\eta_{is,comp}$	85	%	[23]
$\eta_{is,turb}$	90	%	[23]
ε_{HEX}	86	%	[23]
dP_{LTR}	2	%	[23]
dP_{HTR}	3	%	[23]
dP_{DWH}	1	%	[23]
$\Delta T_{pp,GEN}$	3	K	[23]
P_6	74	bar	[23]
SR	0.25	–	[23]
Kalina cycle			
Recuperators temperature difference of pinch point	8	K	[47]
Evaporator temperature difference of pinch point	20	K	[47]
Condensers temperature difference of pinch point	4	K	[47]
Turbine inlet pressure	140	bar	[47]
Working solution ammonia concentration	0.6	–	[47]
Inlet temperature of Kalina turbine	773.15	K	[47]
Pumps isentropic efficiency	70	%	[47]
Turbine isentropic efficiency	85	%	[47]
Basic solution ammonia concentration	0.4037	–	[47]
Inlet temperature of separator, T_{29}	347	K	[47]
Temperature of condenser outlet water	303.15	K	[47]
Temperature of condenser inlet water	293.15	K	[47]
Organic Rankine cycle			
Pinch point temperature difference of condenser	4	K	[48]
Pinch point temperature difference of evaporator	5	K	[48]
Isentropic efficiency of turbine	80	%	[48]
Isentropic efficiency of pump	80	%	[48]
Steam Rankine cycle			
Minimum temperature approach in evaporator	10	K	[49]
Minimum temperature approach in condenser	5	K	[49]
Inlet pressure of the turbine	38.19	bar	[49]
Turbine isentropic efficiency	85	%	[49]
Pump isentropic efficiency	80	%	[49]
PEME			
Cell temperature	353	K	[50]
Cell pressure	1	bar	[50]
Current density (J)	6000	A/m^2	[50]
Active surface area	0.01	m^2	[50]
Membrane thickness (D)	50	μm	[50]

(continued on next page)

Table 1 (*continued*)

Parameter	Value	Unit	Reference
λ_{an}	14	–	[50]
λ_{ca}	10	–	[50]
Cell number	49	–	[50]
Methanation			
Reactor operation temperature	573	K	[51]
Reactor operation pressure	200	bar	[51]
Reactor pressure drop	2	%	[51]
Isentropic efficiency of pumps	85	%	[51]
Efficiency of the HEX7	75	%	[51]
Heat exchangers pressure drop	2	%	[51]
Storage temperature	308	K	[51]
Carbon capture unit			
Compressor adiabatic efficiency	75	%	[52]
Theoretical stages number	10	–	[52]
Operating pressure	4.161	bar	[52]
Top temperature	313.6	K	[52]
Bottom temperature	314.06	K	[52]
TEG			
ZT_m	0.8	–	[50]

where m denotes the molar ratio of air to biomass, and the syngas species formed per mole of feedstock consumed are defined as a_1, a_2, a_3, a_4, a_5, and a_6. Additionally, the mole number of the moisture in the feedstock, denoted w, can be determined as follows [45]:

$$w = \frac{MW_{Biomass} \cdot MC}{MW_{H_2O} \cdot (1 - MC)} \tag{6}$$

where MC denotes moisture content and MW molecular weight.

In order to identify the seven unspecified variables, i.e. m, a_1 , a_2, a_3, a_4, a_5, and a_6, in equation (5), it is necessary to establish seven corresponding equations. The subsequent equations are formulated based on the energy balance principle, the equilibrium relations governing methane production and the water–gas shift reaction, and the elemental balance equations for carbon, hydrogen, oxygen, and nitrogen:

$$a_2 + a_3 + a_5 = 1 \tag{7}$$

$$2a_1 + 2a_4 + 4a_5 = 1.46 + 2w \tag{8}$$

$$a_2 + 2a_3 + a_4 = 0.69 + w + 0.42m \tag{9}$$

$$a_6 = 0.79m \tag{10}$$

From the energy balance of the gasification process, the following additional equation can be derived [45]:

$$\begin{aligned} a_1\overline{h}^0_{H_2} + a_2\overline{h}^0_{CO} + a_3\overline{h}^0_{CO_2} + a_4\overline{h}^0_{H_2O} + a_5\overline{h}^0_{CH_4} + a_6\overline{h}^0_{N_2} - \overline{h}^0_{f,Biomass} - w\overline{h}^0_{f,H_2O(l)} \\ - m\left(0.21\overline{h}^0_{f,O_2} + 0.79\overline{h}^0_{f,N_2}\right) = \dot{Q}_{Gasifier} \end{aligned} \tag{11}$$

Here, $\overline{h}^0_{f,Biomass}$, $\overline{h}^0_{f,H_2O(l)}$, $\overline{h}^0_{f,O_2}$, and $\overline{h}^0_{f,N_2}$ denote the standard formation enthalpies of biomass feedstock, liquid water, oxygen, and nitrogen, respectively. Moreover, $\overline{h}^0$ represents the molar enthalpy of each gaseous species under standard pressure and at the gasifier's operating temperature, while $\dot{Q}_{Gasifier}$ accounts for the heat losses associated with the gasifier [45].

The reduction region of the gasifier involves several key reactions, including the solid–carbon, Boudouard, water–gas shift, and methane formation reactions. These reactions are represented as follows [45]:

$$C + H_2O \leftrightarrow CO + H_2 \tag{12}$$

$$C + CO_2 \leftrightarrow 2CO \tag{13}$$

$$CO + H_2O \leftrightarrow CO_2 + H_2 \tag{14}$$

$$C + 2H_2 \leftrightarrow CH_4 \tag{15}$$

This study focuses particularly on the water–gas shift and methane formation reactions among the various processes taking place in the reduction region. The equilibrium constants corresponding to these reactions are determined using the stoichiometric coefficients given below [45]:

$$K_1 = \frac{P_{CO_2} \cdot P_{H_2}}{P_{CO} \cdot P_{H_2O}} = \frac{a_3 \cdot a_1}{a_2 \cdot a_4}\ K_1^{modified} = A_1.K_1 \tag{16}$$

$$K_2 = \frac{P_{CH_4}}{P^2_{H_2}} = \frac{a_5 \cdot (a_1 + a_2 + a_3 + a_4 + a_5 + a_6)}{a_1^2}\ K_2^{modified} = A_2.K_2 \tag{17}$$

Here, P_i denotes the partial pressure of each gaseous component. To enhance the predictive accuracy of the model, the coefficients $A_1 = 0.91$ and $A_2 = 11.28$ are incorporated into the equilibrium constants corresponding to the water–gas shift and methane formation reactions, respectively. These constants are obtained by comparing the model-predicted gas fractions with experimental data, thereby enhancing the agreement between the model and observed results [56]. The equilibrium constants are subsequently calculated based on the Gibbs free energy of the reactions:

$$K_i\left(T_{Gasifier}\right) = exp\left[-\frac{\Delta\overline{g}_i}{\overline{R}T_{Gasifier}}\right](i = 1, 2) \tag{18}$$

Here, $\overline{R}$ stands for the universal gas constant, which is 8.314 $\frac{kJ}{kmol \cdot K}$, and $T_{Gasifier}$ denotes the gasification temperature. Moreover, the values of $\Delta\overline{g}_i$ are determined for the equilibrium reactions as [45]:

$$\Delta\overline{g}_i = \Delta\overline{h}_i - T_{Gasifier}\Delta\overline{s}_i \tag{19}$$

where

$$\Delta\overline{h}_1 = \overline{h}^0_{CO_2} + \overline{h}^0_{H_2} - \overline{h}^0_{CO} - \overline{h}^0_{H_2O} \tag{20}$$

$$\Delta\overline{h}_2 = \overline{h}^0_{CH_4} - 2\overline{h}^0_{H_2} - \overline{h}^0_{C} \tag{21}$$

$$\Delta\overline{s}_1 = \overline{s}^0_{CO_2} + \overline{s}^0_{H_2} - \overline{s}^0_{CO} - \overline{s}^0_{H_2O} \tag{22}$$

$$\Delta\overline{s}_2 = \overline{s}^0_{CH_4} - 2\overline{s}^0_{H_2} - \overline{s}^0_{C} \tag{23}$$

In previous studies, the actual air-fuel ratio (AF_{act}) has been employed to evaluate the results of gasification process simulations and is determined using the following expression [45]:

$$AF_{act} = \frac{m \cdot MW_{Air}}{MW_{Biomass}} \tag{24}$$

Here, MW_{Air} and m represent the molecular weight of the gasifying air and the molar ratio of air to biomass, respectively. Table 2 illustrates the relationships among the mass, energy, and exergy balance equations within the gasifier.

3.1.2. Combustion chamber

In a combustion reaction, an equivalence ratio (φ) of 1, along with the absence of oxygen in the combustion products, is classified as stoichiometric. In contrast, when the equivalence ratio ranges from 0 to 1, the reaction will generate an excess of oxygen in the products. The chemical reaction of syngas combustion is as follows [45]:

$$\begin{aligned} Syngas + \frac{A_{Stoich}}{\varphi}(0.21O_2 + 0.79N_2) \rightarrow X_{CO_2}CO_2 + X_{H_2O}H_2O + X_{O_2}O_2 \\ + X_{N_2}N_2 \end{aligned} \tag{25}$$

To proceed, the amount of stoichiometric air (A_{Stoich}) is first

Table 2
Energy and exergy balance formulations for the components of the proposed system.

Components	Energy balance equations	Exergy balance equations		
		$\dot{E}_{Fuel}$	$\dot{E}_{Product}$	$\dot{E}_{Loss}$
Biomass				
Gasifier	Presented in section 3.3.1	$\dot{E}_1 + \dot{E}_2$	$\dot{E}_3$	$\dot{Q}_{loss}\left(1 - \frac{T_0}{T_3}\right)$
Combustion Chamber	$\dot{m}_6 = \dot{m}_5 + \dot{m}_4$ $\dot{Q}_{in} = \dot{m}_{NDG} \cdot LHV_{NDG}$ $\dot{Q}_{loss} = 0.02 \cdot \dot{Q}_{in}$	$\dot{E}_4 + \dot{E}_5$	$\dot{E}_6$	$\dot{Q}_{loss}\left(1 - \frac{T_0}{T_6}\right)$
Cooler	$\dot{m}_8(h_8 - h_9) = \dot{m}_{40}(h_{41} - h_{40})$	$\dot{E}_8 - \dot{E}_9$	$\dot{E}_{41} - \dot{E}_{40}$	–
Gas turbine cycle				
Air compressor 1	$\dot{W}_{AC1} = \dot{m}_{11}(h_{11} - h_{10})$	$\dot{W}_{AC1}$	$\dot{E}_{11} - \dot{E}_{10}$	–
Air compressor 2	$\dot{W}_{AC2} = \dot{m}_{13}(h_{13} - h_{12})$	$\dot{W}_{AC2}$	$\dot{E}_{13} - \dot{E}_{12}$	–
Heat exchanger 1	$\dot{m}_{11}(h_{11} - h_{12}) = \dot{m}_{67}(h_{67} - h_{66})$	$\dot{E}_{11} - \dot{E}_{12}$	$\dot{E}_{67} - \dot{E}_{66}$	–
Heat exchanger 2	$\dot{m}_{14}(h_{14} - h_{13}) = \dot{m}_6(h_6 - h_7)$	$\dot{E}_6 - \dot{E}_7$	$\dot{E}_{14} - \dot{E}_{13}$	–
Gas turbine	$\dot{W}_{GT} = \dot{m}_{14}(h_{14} - h_{15})$	$\dot{E}_{14} - \dot{E}_{15}$	$\dot{W}_{GT}$	–
Air preheater	$\dot{m}_{15}(h_{15} - h_{16}) = \dot{m}_4(h_5 - h_4)$	$\dot{E}_{15} - \dot{E}_{16}$	$\dot{E}_5 - \dot{E}_4$	–
Kalina cycle				
Evaporator	$\dot{m}_7(h_7 - h_8) = \dot{m}_{19}(h_{19} - h_{35})$	$\dot{E}_7 - \dot{E}_8$	$\dot{E}_{19} - \dot{E}_{35}$	–
Turbine	$\dot{W}_{TUR} = \dot{m}_{19}(h_{19} - h_{20})$	$\dot{E}_{19} - \dot{E}_{20}$	$\dot{W}_{TUR}$	–
Recuperator 1	$\dot{m}_{20}(h_{20} - h_{21}) = \dot{m}_{35}(h_{35} - h_{34})$	$\dot{E}_{20} - \dot{E}_{21}$	$\dot{E}_{35} - \dot{E}_{34}$	–
Recuperator 2	$\dot{m}_{21}(h_{21} - h_{22}) = \dot{m}_{27}(h_{28} - h_{27})$	$\dot{E}_{21} - \dot{E}_{22}$	$\dot{E}_{28} - \dot{E}_{27}$	–
Condenser 1	$\dot{m}_{23}(h_{23} - h_{24}) = \dot{m}_{36}(h_{37} - h_{36})$	$\dot{E}_{23} - \dot{E}_{24}$	$\dot{E}_{37} - \dot{E}_{36}$	–
Condenser 2	$\dot{m}_{32}(h_{32} - h_{33}) = \dot{m}_{38}(h_{39} - h_{38})$	$\dot{E}_{32} - \dot{E}_{33}$	$\dot{E}_{39} - \dot{E}_{38}$	–
Pump 1	$\dot{W}_{PU1} = \dot{m}_{24}(h_{25} - h_{24})$	$\dot{W}_{PU1}$	$\dot{E}_{25} - \dot{E}_{24}$	–
Pump 2	$\dot{W}_{PU2} = \dot{m}_{33}(h_{34} - h_{33})$	$\dot{W}_{PU2}$	$\dot{E}_{34} - \dot{E}_{33}$	–
Separator	$\dot{m}_{28}h_{28} = \dot{m}_{29}h_{29} + \dot{m}_{30}h_{30}$	$\dot{E}_{28}$	$\dot{E}_{29} + \dot{E}_{30}$	–
Mixer 1	$\dot{m}_{22}h_{22} + \dot{m}_{31}h_{31} = \dot{m}_{23}h_{23}$ $\dot{m}_{23} \cdot x_{23} = \dot{m}_{22} \cdot x_{22} + \dot{m}_{31} \cdot x_{31}$	$\dot{E}_{31} + \dot{E}_{22}$	$\dot{E}_{23}$	–
Mixer 2	$\dot{m}_{26}h_{26} + \dot{m}_{29}h_{29} = \dot{m}_{32}h_{32}$ $\dot{m}_{32} \cdot x_{32} = \dot{m}_{26} \cdot x_{26} + \dot{m}_{29} \cdot x_{29}$	$\dot{E}_{29} + \dot{E}_{26}$	$\dot{E}_{32}$	–
Splitter	$h_{25} = h_{27}, h_{25} = h_{26}$	$\dot{E}_{25}$	$\dot{E}_{27} + \dot{E}_{26}$	–
Throttling valve	$h_{30} = h_{31}$	$\dot{E}_{30}$	$\dot{E}_{31}$	–
Supercritical CO$_2$ cycle				
Main compressor	$\dot{W}_{MC} = (1 - SR) \cdot \dot{m}_{49}(h_{49} - h_{48})$	$\dot{W}_{MC}$	$\dot{E}_{49} - \dot{E}_{48}$	–
Re-compressor	$\dot{W}_{RC} = SR \cdot \dot{m}_{51}(h_{51} - h_{47})$	$\dot{W}_{RC}$	$\dot{E}_{51} - \dot{E}_{47}$	–
Turbine	$\dot{W}_{TUR} = \dot{m}_{42}(h_{42} - h_{43})$	$\dot{E}_{42} - \dot{E}_{43}$	$\dot{W}_{TUR}$	–
High temperature recuperator	$\dot{m}_{52}(h_{53} - h_{52}) = \dot{m}_{43}(h_{43} - h_{44})$ $\varepsilon_{HTR} = \frac{T_{43} - T_{44}}{T_{43} - T_{52}}$	$\dot{E}_{43} - \dot{E}_{44}$	$\dot{E}_{53} - \dot{E}_{52}$	–
Low temperature recuperator	$\dot{m}_{50}(h_{50} - h_{49}) = \dot{m}_{44}(h_{44} - h_{45})$ $\varepsilon_{LTR} = \frac{T_{44} - T_{45}}{T_{44} - T_{49}}$	$\dot{E}_{44} - \dot{E}_{45}$	$\dot{E}_{50} - \dot{E}_{49}$	–
Generator	$\dot{m}_{53}(h_{42} - h_{53}) = \dot{m}_{16}(h_{16} - h_{17})$	$\dot{E}_{16} - \dot{E}_{17}$	$\dot{E}_{42} - \dot{E}_{53}$	–
Mixer	$\dot{m}_{50}h_{50} + \dot{m}_{51}h_{51} = \dot{m}_{52}h_{52}$	$\dot{E}_{50} + \dot{E}_{51}$	$\dot{E}_{52}$	–
Organic Rankine cycle				
Turbine	$\dot{W}_{TUR} = \dot{m}_{54}(h_{54} - h_{55})$	$\dot{E}_{54} - \dot{E}_{55}$	$\dot{W}_{TUR}$	–
Evaporator	$\dot{m}_{46}(h_{46} - h_{48}) = \dot{m}_{57}(h_{54} - h_{57})$	$\dot{E}_{46} - \dot{E}_{48}$	$\dot{E}_{54} - \dot{E}_{57}$	–
Pump	$\dot{W}_{PU} = \dot{m}_{56}(h_{57} - h_{56})$	$\dot{W}_{PU}$	$\dot{E}_{57} - \dot{E}_{56}$	–
Condenser	$\dot{m}_{55}(h_{55} - h_{56}) = \dot{m}_{58}(h_{59} - h_{58})$	$\dot{E}_{55} - \dot{E}_{56}$	$\dot{E}_{59} - \dot{E}_{58}$	–
Steam Rankine cycle				
Evaporator	$\dot{m}_{17}(h_{17} - h_{18}) = \dot{m}_{60}(h_{60} - h_{63})$	$\dot{E}_{17} - \dot{E}_{18}$	$\dot{E}_{60} - \dot{E}_{63}$	–
Turbine	$\dot{W}_{TUR} = \dot{m}_{60}(h_{60} - h_{61})$	$\dot{E}_{60} - \dot{E}_{61}$	$\dot{W}_{TUR}$	–
Pump	$\dot{W}_{PU} = \dot{m}_{63}(h_{63} - h_{62})$	$\dot{W}_{PU}$	$\dot{E}_{63} - \dot{E}_{62}$	–
Condenser	$\dot{m}_{61}(h_{61} - h_{62}) = \dot{m}_{65}(h_{65} - h_{64})$	$\dot{E}_{61} - \dot{E}_{62}$	$\dot{E}_{65} - \dot{E}_{64}$	–

calculated. After defining an equivalence ratio φ, equation (25) is utilized to evaluate the mole fractions of the resulting combustion products (X_i). Here, the equivalence ratio (φ) is described as follows:

$$\varphi = \frac{AF_{Stoich}}{AF_{Actual}} \tag{26}$$

It is assumed that approximately 2 % of the total chemical energy contained in the fuel mixture is lost as heat from the combustion chamber. On the basis of this assumption, the corresponding relationship is derived as follows [45]:

$$\dot{Q}_{Loss,CC} = 0.02 \cdot \dot{m}_{Fuel} \cdot LHV_{Fuel} \tag{27}$$

where $\dot{m}_{Fuel}$ and LHV_{Fuel} denote the fuel mixture's mass flow rate and lower heating value, respectively.

The specific molar chemical exergy of the biomass feedstock is evaluated using the following expression [45]:

$$\bar{e}^{CH}_{Biomass} = \beta \cdot L\overline{H}V_{Biomass} \tag{28}$$

Here, $L\overline{H}V_{Biomass}$ denotes the molar heating value of the biomass feedstock, and β, the coefficient for the chemical exergy of biomass, is computed for solid fuels as follows:

$$\beta = \frac{1.044 + 0.016\frac{M_H}{M_C} - 0.34493\frac{M_O}{M_C}\left(1 + 0.0531\frac{M_H}{M_C}\right)}{1 - 0.4124\frac{M_O}{M_C}} \tag{29}$$

Here, M_H, M_C, and M_O denote the mass fractions of hydrogen, carbon, and oxygen in the biomass, respectively. The corresponding energy and exergy balance relations for the combustion chamber are given in Table 2, which also presents the syngas stream expressed as normal dry gas (NDG).

Also, Table 2 provides the energy and exergy balance relations for the subsystems of the power cycle.

3.1.3. Thermoelectric generator (TEG)

The thermoelectric generator (TEG) equations associated with the current conditions are denotable as [50]:

$$\eta_{Teg} = \frac{\sqrt{1+ZT_m}-1}{\sqrt{1+ZT_m}+\frac{T_L}{T_H}} \tag{30}$$

The temperatures at the cold and hot surfaces of the TEG are represented by T_L and T_H , respectively. The dimensionless figure of merit, ZT_m, generally ranges from 0.2 to 1.6, depending on the material selection. For present study, a baseline value of 0.8 is considered for bismuth telluride. Based on these values, the corresponding Carnot efficiency can be expressed as [50]:

$$\eta_{carnot} = \frac{T_L}{T_H} \tag{31}$$

from which the following beneficial quantity is obtained [50]:

$$\eta_{TEG} = \frac{\dot{W}_{TEG}}{\dot{Q}_{Elegant}} \tag{32}$$

Here, $\dot{W}_{TEG}$ is the work produced by the TEG, while $\dot{Q}_{Elegant}$ refers to the device responsible for efficiently converting a liquid-based energy source into electricity. For the TEG, this is expressed as follows [50]:

$$\dot{Q}_{Elegant} = \dot{m}_{cooling}\left(h_{cold,in} - h_{cold,out}\right) \tag{33}$$

where $\dot{m}_{cooling}$ denotes the mass flow rate on the TEG's cold surface, $h_{cold,in}$ is the enthalpy of the coolant entering the cold side, and $h_{cold,out}$ is the enthalpy of the coolant leaving the cold side. By employing an appropriate approximation, the effective cold- and hot-side temperatures of the TEG are estimated using the average inlet temperatures of the hot and cold streams, as commonly applied in the literature to represent the actual temperature difference for Carnot efficiency estimation. Thus, the cold and hot side temperatures are calculated respectively as follows [50]:

$$T_L = \frac{1}{2}\left(T_{cold,in} + T_{cold,out}\right) \tag{34}$$

$$T_H = \frac{1}{2}\left(T_{Hot,in} + T_{Hot,out}\right) \tag{35}$$

3.1.4. Carbon capture unit

Modeling and simulation of the CO_2 absorption process using monoethanolamine as a solvent were done by Aspen HYSYS. This simulation was meant to model the absorption and subsequent separation of CO_2 from the exhaust gas stream and the subsequent regeneration of the solvent. The basic unit operations in the process flow diagram included a compressor (COMP), a heat exchanger (HEX3), an absorption column (ABS), and a flash vessel (THV), for solvent regeneration and a separator (SEP) for separating CO_2 and solvent. The components used for the simulation included CO_2, MEA, water, and other relevant gases present in the inlet stream. The ACID GAS property package was used for thermodynamic calculations in view of its reliable performance in amine-based CO_2 capture systems. This package incorporates the electrolyte NRTL model to describe liquid phase properties and uses the Peng-Robinson equation of state to model vapor phase behavior to provide an accurate representation of the complex vapor-liquid equilibria in the CO_2-MEA-H_2O system. The simulation was based on a sequential modular approach with tight convergence criteria to ensure accuracy and stability of solutions. Various sensitivity analyses were performed on main process variables: MEA concentration, gas-to-liquid ratio in the absorber, and regeneration conditions, to optimize the whole process performance. CO_2 capture efficiency, energy consumption, and the effectiveness of solvent regeneration have been major indicators studied herein.

Also, the chemical reaction between MEA and CO_2 in the process of absorption can be expressed by the following overall reaction [52]:

$$CO_2 + RNH_2 \rightarrow RNH_3^+ + HCO_3^- \tag{36}$$

where R stands for the ethanol group, CH_2CH_2OH, in MEA. This reaction is irreversible as far as the conditions existing in the absorption column are concerned. The reaction is exothermic and ultimately gives the protonated MEA RNH_3^+ and the bicarbonate ion, HCO_3^-. The reaction occurs in the liquid solution of MEA where CO_2 is being captured from the gas phase. The irreversible reaction above represents the essence of CO_2 capture in the MEA-based absorption process. The carbon capture efficiency can also be calculated as follows:

$$\text{Carbon capture efficiency }(\%) = \frac{\text{Captured } CO_2}{\text{Total } CO_2 \text{ emissions}} \times 100 \tag{37}$$

3.1.5. Wastewater treatment unit

Integrating wastewater treatment into the proposed polygeneration system is strategically advantageous, as the thermal section of the system naturally generates substantial waste heat during gasification, methanation, and other high-temperature processes. Instead of being released unused, this low-to medium-grade waste heat is recovered and utilized to drive the multi-stage thermal separation process, significantly reducing the external energy demand of wastewater purification. This energy synergy not only enhances the overall efficiency of the polygeneration system but also mitigates one of the primary cost barriers associated with wastewater treatment, which is traditionally highly energy-intensive. Moreover, coupling wastewater treatment with biomass gasification and carbon-utilization processes enables centralized management of both gaseous and aqueous pollutants. Such centralization avoids the need for separate standalone units, each requiring dedicated energy supply and additional infrastructure, which would otherwise increase operational costs and environmental impacts. By recovering waste heat and consolidating resource flows, the integrated configuration supports a more sustainable, circular, and cost-effective urban energy–water–waste nexus.

The methodology employed in this wastewater treatment unit is a thermal separation technique that utilizes the latent heat of vaporization and condensation to purify water. It relies on the selective evaporation of water molecules, achieved by applying heat to convert contaminated water into steam, thereby separating it from dissolved impurities such as minerals and salts. The method involves transferring heat from a clean steam source to the contaminated water, followed by controlled condensation of the resulting pure steam in a separate environment. A multi-stage approach is adopted to enhance efficiency, where heat is reused across stages to maximize energy utilization and improve purification outcomes. This technique is particularly effective for treating water with high impurity concentrations, such as seawater or urban wastewater, and is optimized to produce high-quality water for sensitive

Table 3
Average chemical composition of typical urban wastewater.

Constituent	Concentration (ppm)
NO_3-N	3.9
NH_4-N	4.1
PO_4	8.6
K	22.4
Ca	99.03
Mg	84.19
Na	275.25
Cl	93.2
Fe	0.72
Mn	0.061
Zn	0.039
Cu	0.09
Pb	0.023
Ni	0.01
Cd	Not detectable

applications. Table 3 represents the average chemical composition of typical wastewater with pH of 7.8.

3.1.6. PEM electrolyzer

In a PEM electrolyzer, water undergoes electrochemical splitting into hydrogen and oxygen through the application of both electrical and thermal energy. As illustrated by the following reaction, hydrogen is produced at the cathode, whereas oxygen is released at the anode [50]:

$$H_2O \rightarrow H_2 + 0.5O_2 \tag{38}$$

The required energy for hydrogen production can be expressed as [50]:

$$\Delta H = \Delta G + T\Delta S \tag{39}$$

Here, ΔG denotes the electrical energy required (Gibbs free energy), whereas TΔS indicates the heat needed per mole of hydrogen (J/mol H_2). The overall energy requirement reflects the theoretical input for water electrolysis, without accounting for practical system losses. The hydrogen production molar flow rate is then calculated as follows [50]:

$$\dot{n}_{H_{2,out}} = \frac{J}{2F} = \dot{n}_{H_2O,react} \tag{40}$$

The current density J governs the production rates in the electrolysis unit. According to equation (38), the molar generation rate of oxygen is equal to half that of hydrogen. Based on this relationship, the outlet molar flow rates of oxygen and water from the electrolysis unit can be evaluated:

$$\dot{n}_{O_{2,out}} = \frac{J}{4F} \tag{41}$$

$$\dot{n}_{H_2O,out} = \dot{n}_{H_2O,in} - \frac{J}{2F} \tag{42}$$

The necessary electrical energy is formulated as follows:

$$E_{electric} = J \times V \tag{43}$$

Here, $E_{electric}$ represents the input energy, while the parameter V denotes the cell potential, which can be written as follows [50]:

$$V = V_0 + V_{act,ca} + V_{act,an} + V_{ohm} \tag{44}$$

Here, $V_{act,ca}$, $V_{act,an}$, and V_{ohm} denote the activation overpotentials at the cathode and anode, as well as the ohmic overpotential, respectively. The reversible potential, V_0 is calculated using the Nernst equation. Additional details about the overpotentials and the Nernst equation are provided in Table 4.

Table 4
Electrical equations for PEM electrolyzer [50].

Term	Equation
Nernst equation	$V_0 = 1.229 - 0.00085(T_{PEME} - 298)$
Anod overpotential equation	$V_{act,an} = \frac{RF}{T}\sinh^{-1}\frac{J}{2J_{0,an}}$ $J_{0,an} = J_{an}^{ref}\exp\left(\frac{-E_{act,an}}{\overline{R}T}\right)$ $E_{act,an} = 76kJ/mole$
Cathode overpotential equation	$V_{act,ca} = \frac{RF}{T}\sinh^{-1}\frac{J}{2J_{0,ca}}$ $J_{0,an} = J_{ca}^{ref}\exp\left(\frac{-E_{act,ca}}{\overline{R}T}\right)$ $E_{act,an} = 18kJ/mole$
Ohmic overpotential equation	$V_{ohm} = J \times R_{PEME}$ $R_{PEME} = \int_0^D \frac{dx}{\sigma_{PEME}[\lambda(x)]}$ $\lambda(x) = \frac{\lambda_{an} - \lambda_{ca}}{D}x + \lambda_{ca}$ $\sigma_{PEME}[\lambda(x)] = [0.5139\,\lambda(x) - 0.326]exp\left[1268\left(\frac{1}{303} - \frac{1}{T_{PEME}}\right)\right]$

3.1.7. Methanation subsystem

Methanation refers to the catalytic reaction between carbon dioxide and hydrogen, commonly described by the Sabatier process. Two main reaction pathways for this process have been reported. According to the first pathway, methane is synthesized through the direct hydrogenation of CO_2, as expressed below [51]:

$$CO_2 + 4H_2 \leftrightarrow CH_4 + 2H_2O\ \Delta H = -164.9\ kJ/mole \tag{45}$$

In a more prevalent mechanism occurring in two stages, carbon monoxide is initially generated through the water-gas shift reaction, followed by the production of methane via the hydrogenation of carbon monoxide, as demonstrated respectively as [51]:

$$CO_2 + H_2 \leftrightarrow CO + H_2O\ \Delta H = 41.5\ kJ/mole \tag{46}$$

$$CO + 3H_2 \leftrightarrow CH_4 + H_2O\ \Delta H = -206.4\ kJ/mole \tag{47}$$

Methane is produced via the exothermic hydrogenation of CO_2, which typically occurs between 200 and 550 °C depending on the catalyst and is also influenced by pressure. Research indicates that CO_2 conversion improves with higher pressure and lower temperature, with temperature having the greater effect [51]. In this study, methanation is modeled using a Ru-catalyzed membrane reactor, following Ohya et al. [57]. Ruthenium provides high activity and selectivity for converting syngas to methane. The reactor combines a catalytic unit with a vapor-perm-selective membrane, enabling internal separation of steam and syngas, resulting in approximately 18 % higher CO_2 conversion compared to conventional reactors. The Sabatier reactor model applies an experimentally derived correlation linking CO_2 conversion to reaction temperature (T_{sab}) [51]:

$$CR_{SM}(\%) = 39.25 + \left[0.333 \times (T_{sab} - 273.15) + \left(-0.0005 \times (T_{sab} - 273.15)^2\right)\right] \tag{48}$$

where CR_{SM} represents the conversion fraction of CO_2, and the amount of methane formed is obtained as the product of the inlet molar flow of CO_2 and its conversion fraction within the reactor [51]:

$$\dot{n}_{CH_4,out} = CR_{SM} \times \dot{n}_{CO_2,in} \tag{49}$$

Considering the stoichiometric relationships, the outlet mole fractions (x_i) of the reactor components are determined as follows [51]:

$$\dot{n}_{g,out} = \left(\dot{n}_{CO_2,in} + \dot{n}_{H_2,in}\right) - 2 \times \dot{n}_{CH_4,out} \tag{50}$$

$$X_{CO_2,out} = \frac{\left(\dot{n}_{CO_2,in} - \dot{n}_{CH_4,out}\right)}{\dot{n}_{g,out}} \tag{51}$$

$$X_{H_2,out} = \frac{\left(\dot{n}_{H_2,in} - 4 \times \dot{n}_{CH_4,out}\right)}{\dot{n}_{g,out}} \tag{52}$$

$$X_{CH_4,out} = \frac{\left(\dot{n}_{CH_4,in} - \dot{n}_{CH_4,out}\right)}{\dot{n}_{g,out}} \tag{53}$$

Fig. 2 illustrates the overall workflow of the system analysis, detailing the sequential steps from initial simulation to final evaluation. The first and second laws of thermodynamics are applied to evaluate the energy and exergy efficiencies of the proposed polygeneration system:

$$\eta_I = \frac{\dot{W}_{net} + \dot{Q}_{DWH} + \dot{m}_{CH4}\ LHV_{CH4} + \dot{m}_{H2}\ LHV_{H2}}{\dot{m}_{MSW}LHV_{MSW}} \tag{54}$$

$$\eta_{II} = \frac{\dot{W}_{net} + \dot{E}_{Q,DWH} + \dot{E}_{CH4} + \dot{E}_{H2}}{\dot{E}_{MSW}} \tag{55}$$

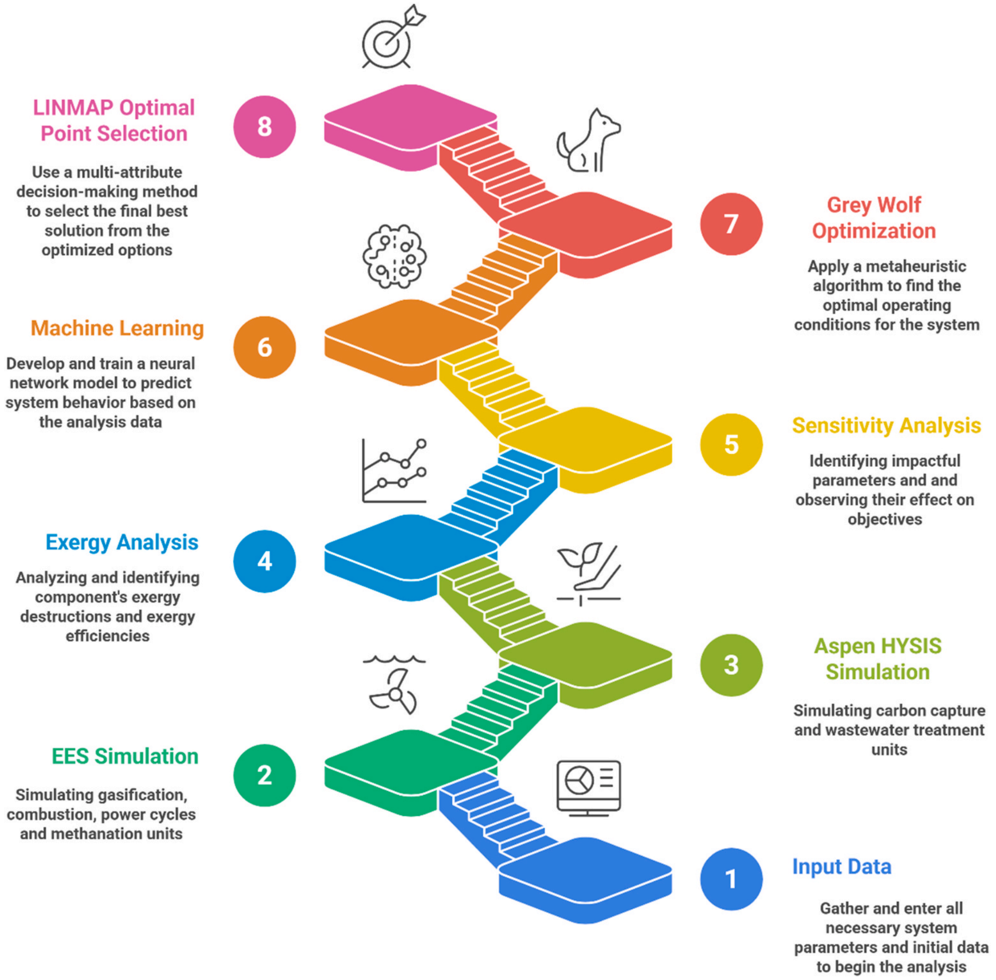

Fig. 2. Workflow of the simulation and analysis procedure.

3.2. *Multi-objective optimization*

Optimizing system operation is important for achieving sustainable development. To verify this, an extensive sensitivity analysis was performed to identify the parameters exerting the most significant influence on overall system performance, as outlined in Table 5. The energy and exergy efficiencies, along with the hydrogen generation rate, were defined as the objective functions for the multi-objective optimization. The sensitivity results guided the selection of the most influential variables for the optimization study. A dataset of 1200 randomly generated samples was then used to train artificial neural networks (ANNs) that model the system's behavior. These ANNs facilitated the use of the multi-objective grey wolf optimizer (MOGWO), a metaheuristic method that emulates the cooperative social behavior and hunting strategy of grey wolves. Fig. 3 outlines the workflow used for the machine-learning-based optimization. The predictive performance of the ANNs is illustrated in Fig. 4, while the optimization results for the three objectives are presented in Fig. 5. Finally, the LINMAP method was employed to choose a single solution from the Pareto-optimal set, providing the most balanced outcome by considering all objectives and their associated trade-offs.

Table 5
Variables under consideration and their ranges of possible values.

Decision variable	Range of variation
Air compressor 1 pressure ratio	2–4
Air compressor 2 pressure ratio	2–4
Gas turbine inlet temperature (K)	1300–1600
Kalina evaporator pinch-point difference	10–40
Main compressor pressure ratio	2–4
Re-compressor pressure ratio	2–4
PEME cell number	40–60

4. Results

This section presents the study's key findings, beginning with the validation of the mathematical model against established data. The subsequent analysis includes detailed energy and exergy assessments, a sensitivity analysis of key parameters, and the results of a multi-objective optimization.

4.1. *Model validation*

The investigated system's subsystems were validated by comparing the mathematical model results with data from the previous studies under similar conditions, highlighting close agreement. The validation tables and figures are provided in the supplementary material (see Table S1–S4 and Fig. S1–S2).

4.2. *Energy and exergy assessment outcomes*

Tables 6–9 display the outcomes of the thermodynamic examination applied to the proposed polygeneration system's power cycles, wastewater treatment unit and PEME, carbon capture unit, and methanation unit under design condition, respectively. The examination takes into account energy and exergy relationships, input data in Table 1, and

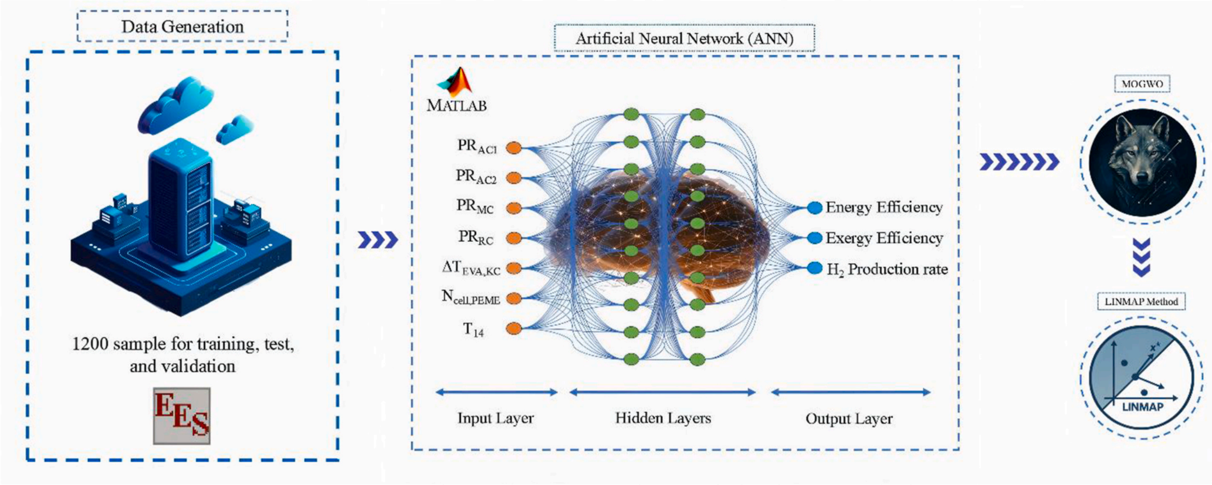

Fig. 3. Optimization process implemented in this study.

relies on the assumptions mentioned earlier.

Table 10 presents a comprehensive exergy analysis, detailing the fuel, product, and destruction rates alongside the exergy efficiencies for all system components. The analysis reveals that the biomass subsystem is the most significant source of irreversibility, accounting for approximately 54.0 % of the system's total exergy destruction. Within this critical subsystem, the gasifier is the dominant contributor, exhibiting substantial exergy destruction rate of 8014 kW and an exergy efficiency of 57.7 %, which highlights the inherent thermodynamic losses during the gasification process. Although the combustion chamber achieves a relatively high exergy efficiency of 90.2 %, it still experiences a considerable exergy destruction rate, totaling 1166 kW. In a notable contrast, the cooler, while having the lowest exergy destruction rate at 45.4 kW, also demonstrates the poorest exergy efficiency at just 38.3 %.

In the gas turbine cycle, the primary source of thermodynamic loss is identified in Heat Exchanger 2, which undergoes substantial exergy destruction rate of 1384 kW at an efficiency of 83.0 %, indicating significant irreversibilities during the heat transfer process. The gas turbine itself operates with a high exergy efficiency of 96.6 %; however, it still contributes a non-negligible 148.4 kW exergy destruction rate. Conversely, Air Compressor 2 demonstrates superior performance with the lowest exergy destruction rate in the cycle at 33.7 kW, coupled with a high exergy efficiency of 89.4 %. The air preheater also contributes significantly to the cycle's overall losses, with a 549.5 kW exergy destruction rate and an exergy efficiency of 64.4 %.

Within the Kalina cycle, the evaporator and turbine are the main drivers of exergy loss, with destruction rates of 224.4 kW and 181.6 kW, respectively. The evaporator's efficiency of 88.2 % reflects notable losses during the phase-change process. Condenser 1 emerges as the least efficient component in this cycle, with an exergy efficiency of only 30.8 % and an exergy destruction rate of 66.6 kW, which points to significant inefficiencies in the heat rejection mechanism. In stark contrast, the splitter and mixer components exhibit near-perfect exergy efficiencies of 100 % and approximately 99.95–99.98 %, with minimal destruction rates. This exceptional performance is a result of their modeling as ideal, isolated units that assume no heat transfer or pressure drop. The mixer's high efficiency is further explained by the fact that the combining streams possess nearly identical temperatures and pressures, minimizing the thermodynamic driving force for exergy destruction. Moreover, in the Kalina cycle, where the working fluid concentration is variable, both physical and chemical exergy are considered. Their combined effect yields a total exergy ratio close to unity, which contributes to the observed high efficiencies of these components.

In the supercritical CO_2 cycle, the primary source of thermodynamic loss is identified in the low-temperature recuperator, which exhibits the highest exergy destruction rate at 63.3 kW with an efficiency of 86.5 %, suggesting moderate irreversibilities during the heat recovery process. The turbine operates with a high degree of efficiency at 95.6 %, though it still contributes a 43.9 kW exergy destruction rate. The main compressor and re-compressor also maintain strong performance, with high exergy efficiencies of 88.9 % and 91.8 % and correspondingly low destruction rates of 32.1 kW and 15.6 kW, respectively. In contrast, the mixer demonstrates ideal performance with a negligible exergy destruction rate (0.054 kW) and a perfect exergy efficiency of 100 %.

Within the Organic Rankine Cycle (ORC), the evaporator is the primary contributor to exergy loss, recording a substantial destruction rate of 63.2 kW at an efficiency of 71.8 %, which indicates significant losses during the heat absorption phase. The turbine follows as the next most significant source of loss, with a 38.8 kW exergy destruction rate and an exergy efficiency of 81.5 %. Conversely, the pump and condenser exhibit minimal exergy destruction rates (0.11 kW and 1.72 kW, respectively) and maintain relatively high exergy efficiencies (80.3 % and 87.6 %), reflecting their efficient operation within the cycle.

The analysis of the Steam Rankine Cycle (SRC) reveals that the turbine and condenser are the main areas for potential improvement. The turbine exhibits a substantial exergy destruction rate of 160.7 kW and an efficiency of 85.6 %, reflecting notable losses during the expansion process. The condenser is identified as the least efficient component, with a low exergy efficiency of just 34.3 % alongside a 67.5 kW exergy destruction rate, which points to significant inefficiencies in the heat rejection mechanism. The evaporator performs more effectively, with a lower destruction rate of 57.77 kW and a high exergy efficiency of 95.3 %, while the pump operates effectively with very low destruction rate (0.92 kW) and an efficiency of 81.0 %.

In the wastewater treatment unit, Heat Exchanger 5 is a critical point of inefficiency, exhibiting a disproportionately high exergy destruction rate of 3634 kW and a relatively low exergy efficiency of 62.4 %. This starkly contrasts with the performance of Heat Exchanger 4, which demonstrates a much higher efficiency of 98.7 % with a significantly lower destruction rate of 127 kW. The other components in this unit, including the throttling valve, separator 2, and mixer, have low destruction rates and high exergy efficiencies, indicating reliable and effective operation.

The carbon capture unit's exergy analysis highlights severe inefficiencies in the throttling valve, which records the highest exergy destruction rate at 388.7 kW but a very low exergy efficiency of only 28.3 %. This reflects the significant thermodynamic penalties associated with the pressure reduction process. Heat Exchanger 3 is the next largest contributor, with a 281 kW exergy destruction rate and an efficiency of 78.1 %. The compressor and absorber column show moderate exergy

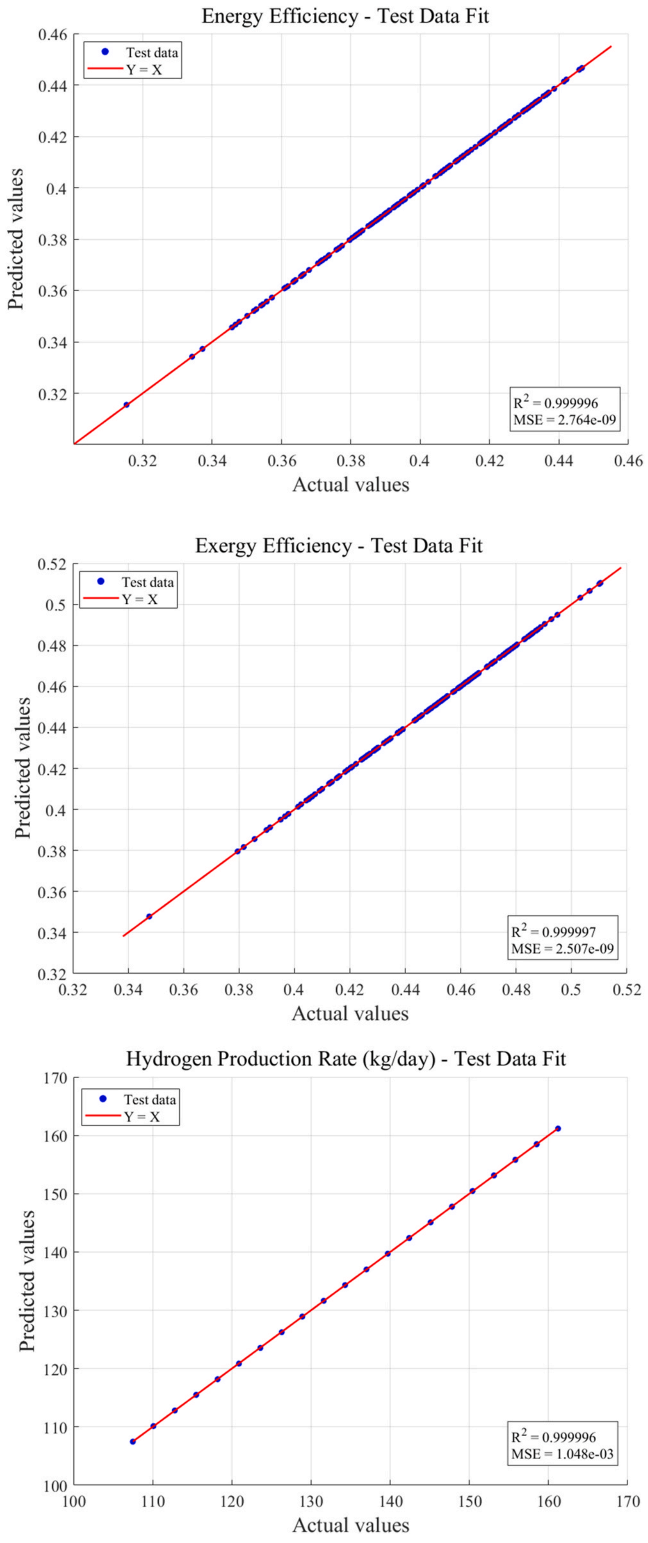

Fig. 4. Accuracy of ANN predictions for the different objective functions.

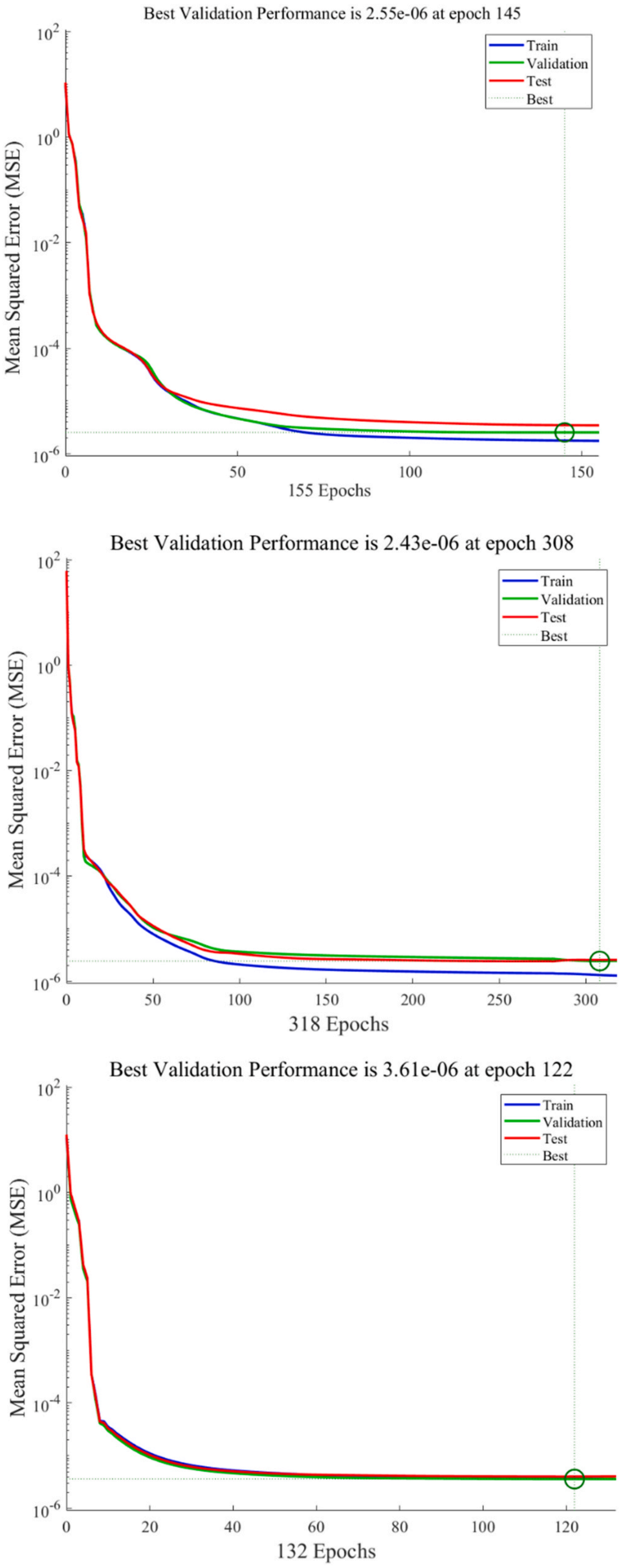

Fig. 5. Neural network performance curves for each selected objective.

loss rates (228.8 kW and 157.8 kW) with more respectable exergy efficiencies of 84.8 % and 87.9 %, respectively, while the separator exhibits the lowest destruction rate but a modest efficiency of 46.5 %.

Finally, in the methanation unit, the Sabatier reactor is the main source of exergy loss, exhibiting a destruction rate of 18.4 kW with an exergy efficiency of 90.2 %, which indicates moderate losses during the chemical reaction processes. The ancillary components, including heat exchangers 6, 7, and 8 and pumps 3 and 4, exhibit very low exergy destruction rates (e.g., 0.0033 kW for heat exchanger 6 and 0.1612 kW for pump 3) and high exergy efficiencies ranging from 62.3 % to 98.1 %. The mixer within this unit operates ideally, with zero exergy destruction and a perfect 100 % exergy efficiency.

Fig. 6 illustrates the proportion of exergy destruction in each

Table 6
Thermodynamic properties of proposed system.

State	Working fluid	$T(K)$	P(bar)	x (−)	$\dot{m}$(kg /s)	h(kJ /kg)	s(kJ /kg.K)	$\dot{E}$(kW)
1	Air	293.2	1.013	–	2.71	0	0	14.52
2	MSW	293.2	1.013	–	1.155	–	–	18908
3	Syngas	823	1.013	–	3.683	−2882	1.794	10908
4	Air	293.2	1.013	–	3.853	293.3	6.843	20.65
5	Air	847.8	1.013	–	3.853	875.1	7.947	1015
6	Exhaust gas	1877	1.013	–	7.536	−989.7	2.497	10757
7	Exhaust gas	826.2	1.013	–	7.536	−2383	1.42	2635
8	Exhaust gas	379.1	1.013	–	7.536	−2894	0.5359	734.9
9	Exhaust gas	323.1	1.013	–	7.536	−2954	0.3658	661.4
10	Air	293.2	1.013	–	8.268	293.3	6.843	0
11	Air	383.5	2.323	–	8.268	384.3	6.874	676
12	Air	280	2.288	–	8.268	279.8	6.561	571.2
13	Air	366.5	5.263	–	8.268	366.6	6.592	1213
14	Air	1500	5.105	–	8.268	1637	8.145	7951
15	Air	1066	1.013	–	8.268	1122	8.206	3550
16	Air	826.2	1.013	–	8.268	851.2	7.918	2006
17	Air	672	1.013	–	8.268	683.6	7.694	1164
18	Air	313.2	1.013	–	8.268	313.5	6.909	5.433
19	NH_3H_2O	773.2	140	0.6	1.436	2854	6.215	19146
20	NH_3H_2O	369.3	1.688	0.6	1.436	1967	6.646	17690
21	NH_3H_2O	359.6	1.688	0.6	1.436	1701	5.911	17617
22	NH_3H_2O	315.6	1.688	0.6	1.436	630.4	2.79	17394
23	NH_3H_2O	321.1	1.688	0.4037	4.222	299.2	1.587	35122
24	NH_3H_2O	297.2	1.688	0.4037	4.222	−122	0.2283	35026
25	NH_3H_2O	297.2	4.66	0.4037	4.222	−121.5	0.2288	35028
26	NH_3H_2O	297.2	4.66	0.4037	0.9181	−121.5	0.2288	7618
27	NH_3H_2O	297.2	4.66	0.4037	3.303	−121.5	0.2288	27410
28	NH_3H_2O	347	4.66	0.4037	3.303	343.9	1.637	27583
29	NH_3H_2O	347	4.66	0.9478	0.5182	1502	5.323	9842
30	NH_3H_2O	347	4.66	0.3025	2.785	128.4	0.9516	17734
31	NH_3H_2O	323.5	1.688	0.3025	2.785	128.4	0.9656	17722
32	NH_3H_2O	325.6	4.66	0.6	1.436	464.3	2.086	17452
33	NH_3H_2O	297.2	4.66	0.6	1.436	−119.5	0.2079	17404
34	NH_3H_2O	300	140	0.6	1.436	−95.02	0.2324	17429
35	NH_3H_2O	358.2	140	0.6	1.436	171.2	1.042	17470
36	Water	293.2	1.013	–	42.51	83.93	0.2962	22391
37	Water	303.2	1.013	–	42.51	125.8	0.4365	22421
38	Water	293.2	1.013	–	20.04	83.93	0.2962	10559
39	Water	303.2	1.013	–	20.04	125.8	0.4365	10573
40	Water	293.2	1.013	–	2.684	83.93	0.2962	0
41	Water	333.2	1.013	–	2.684	251.2	0.8311	28.11
42	CO_2	823.2	198.5	–	7.332	528.5	0.00376	3871
43	CO_2	706.1	74	–	7.332	399.8	0.02419	2883
44	CO_2	561.6	71.78	–	7.332	234.9	−0.2313	2223
45	CO_2	421.3	70.34	–	7.332	77.83	−0.5495	1756
46	CO_2	421.3	70.34	–	5.499	77.83	−0.5495	1317
47	CO_2	421.3	70.34	–	1.833	77.83	−0.5495	438.9
48	CO_2	308.2	68.94	–	5.499	−86.27	−1.01	1156
49	CO_2	398.5	213	–	5.499	−33.59	−0.9899	1414
50	CO_2	536.2	208.8	–	5.499	172.2	−0.5386	1818
51	CO_2	543.8	208.8	–	1.833	182	−0.5205	614.2
52	CO_2	538.1	208.8	–	7.332	174.6	−0.5341	2432
53	CO_2	670	202.5	–	7.332	339.6	−0.2541	3040
54	Toluene	416.3	2.36	–	1.597	405.4	0.9797	223.9
55	Toluene	334.4	0.036	–	1.597	298.2	1.063	13.82
56	Toluene	297.2	0.036	–	1.597	−159.9	−0.4703	−0.1063
57	Toluene	297.2	2.36	–	1.597	−159.6	−0.47	0.3251
58	Water	293.2	1.013	–	17.49	83.93	0.2962	0
59	Water	303.2	1.013	–	17.49	125.8	0.4365	12.2
60	Steam	662	38.19	–	1.007	3190	6.754	1222
61	Steam	308.2	0.056	–	1.007	2240	7.298	104.1
62	Steam	308.2	0.056	–	1.007	146.6	0.505	1.468
63	Steam	308.5	38.19	–	1.007	151.4	0.5081	5.376
64	Water	293.2	1.013	–	50.4	83.93	0.2962	0
65	Water	303.2	1.013	–	50.4	125.8	0.4365	35.16
66	Water	293.2	1.013	–	5.165	83.93	0.2962	0
67	Water	333.2	1.013	–	5.165	251.2	0.8311	54.08

subsystem and component. The integrated system has an overall exergy destruction of approximately 17800 kW across its subsystems, with the Biomass subsystem contributing the highest losses at 9776 kW, accounting for roughly 54.0 % of the total due to its energy-intensive processes. The Wastewater treatment unit follows with significant losses at 3904 kW, and the PEME subsystem adds a notable 289.3 kW to the total exergy destruction. In contrast, the Methanation unit demonstrates the lowest exergy destruction at 19 kW, reflecting its highly efficient operation, while the ORC also performs well with relatively low losses at 103.8 kW.

Table 7
Thermodynamic properties of wastewater treatment unit and PEME.

State	$T(K)$	P(bar)	h(kJ/kg)	s(kJ/kg.K)	$\dot{m}$(kg/s)	Mass fraction				
						H_2O	Ammonia	NaCl	H_2	O_2
Wastewater treatment unit										
68	293.2	1.013	−15870	3.001	1.4975	0.999	~0	0.001	–	–
69	373	1.013	−13290	10.06	0.6691	0.9999	0.0001	~0	–	–
70	373	1.013	−15550	3.973	0.8283	0.9982	0.0001	0.0017	–	–
71	372.7	1.013	−13180	9.95	0.6691	0.9999	0.0001	~0	–	–
72	358.9	0.6	−15550	3.976	0.8283	0.9982	0.0001	0.0017	–	–
73	358.9	0.6	−15620	3.754	0.1474	0.9901	0.001	0.0089	–	–
74	358.9	0.6	−13310	10.23	0.6808	1	0	0	–	–
75	359	0.6	−14420	7.133	1.3503	1	0	0	–	–
76	293.2	1.013	83.93	0.2962	0.7869	1	0	0	–	–
77	303.2	1.01	125.8	0.4365	0.7869	1	0	0	–	–
78	353.2	1.013	−15630	3.762	1.3503	1	0	0	–	–
PEM electrolyzer unit										
79	353.2	1.013	50.8	0.1572	0.02438	–	–	–	0	1
80	353.2	1.013	4723	55.82	0.003047	–	–	–	1	0

Table 8
Thermodynamic properties of carbon capture unit.

State	$T(K)$	P(bar)	h(kJ/kg)	s(kJ/kg.K)	$\dot{m}$(kg/s)	Mass fraction				
						CO_2	MEA	N_2	O_2	H_2O
81	511.3	4.16	−3185	5.442	7.536	0.3171	0	0.6023	0.0379	0.0426
82	323.2	4.16	−3448	4.767	7.536	0.3171	0	0.6023	0.0379	0.0426
83	313.2	4.16	−4332	0.1744	285.8	0	1	0	0	0
84	313.26	4.16	−393.5	4.915	4.91	0.0453	0.0009	0.8993	0.0545	0
85	314.1	4.16	−4376	0.2167	288.3	0.0075	0.9909	0.0004	0.0001	0.0011
86	313.65	0.15	−4376	0.2212	288.3	0.0075	0.9909	0.004	0.0001	0.0011
87	313.65	0.15	−4348	0.1902	286.4	0.0010	0.9979	0	0	0.0011
88	313.65	0.15	−8251	4.532	2.0575	0.9102	0.0156	0.0589	0.0101	0.0051
89	313.65	0.15	−8251	4.532	2.0409	0.9102	0.0156	0.0589	0.0101	0.0051
90	313.65	0.15	−8251	4.532	0.01663	0.9102	0.0156	0.0589	0.0101	0.0051

Table 9
Thermodynamic properties of methanation unit.

State	$T(K)$	P(bar)	h(kJ/kg)	s(kJ/kg.K)	$\dot{m}$(kg/s)	Mass fraction			
						CO_2	H_2	CH_4	H_2O
91	563.3	2.041	253.8	0.47	0.008315	1	0	0	0
92	523	2	211.7	0.3964	0.008315	1	0	0	0
93	447.7	2.041	6091	56.27	0.001524	0	1	0	0
94	502.1	2.041	6881	58.02	0.001524	0	1	0	0
95	523	2	7184	58.69	0.00152	0	1	0	0
96	523	2	377.7	2.756	0.009838	0.7318	0.2682	0	0
97	573	1.96	853.6	2.772	0.003429	0.142	0.2601	0.832	0
98	529.6	1.92	719.1	2.539	0.003429	0.142	0.2601	0.832	0
99	562.7	1.882	821.2	2.737	0.003429	0.142	0.2601	0.832	0
100	308	20.26	107.3	−0.273	0.003429	0.142	0.2601	0.832	0
101	573	1.96	3071	7.901	0.006366	0	0	0	1
102	479	1.92	2882	7.55	0.006366	0	0	0	1
103	353.2	1.013	4723	55.82	0.001524	0	1	0	0

Table 11 summarizes the performance indicators of the integrated polygeneration system at baseline operating conditions. The system has energy and exergy efficiencies of 35.0 % and 39.9 %, respectively, reflecting moderate thermodynamic performance. Key outputs include the net power generation of 3510 kW, heating production of 1310 kW, methane production rate at 296.3 kg/day, hydrogen production rate at 131.6 kg/day, and oxygen production rate at 2106 kg/day. The carbon capture unit demonstrates strong environmental performance by capturing approximately 87 % of CO_2 emissions from the exhaust gases, corresponding to a substantial capture rate of 177.8 tons per day. This significantly mitigates greenhouse gas emissions and contributes to the reduction of the system's overall carbon footprint. In parallel, the integrated wastewater treatment unit processes 116.6 m^3 of wastewater per day, playing a vital role in sustainable water management and environmental protection. Together, these subsystems enhance the environmental sustainability of the proposed polygeneration system by effectively managing emissions and waste streams.

4.3. Fuel production performance across multiple scenarios

Three fuel production scenarios are evaluated: hydrogen-only, methane-only, and dual-fuel production. The primary goal is to match fuel output with market demand for both methane and hydrogen. As illustrated in Fig. 7, under the methane-only scenario, the system achieves an energy efficiency of 34.87 % and an exergy efficiency of 39.83 %. In contrast, the hydrogen-only scenario obtains an energy efficiency

Table 10
Exergy analysis results of the system components.

Component	$\dot{E}_{Fuel}$	$\dot{E}_{Product}$	$\dot{E}_{Destruction}$	ε (%)
Biomass				
Gasifier	18923	10908	8014	57.7
Combustion chamber	11923	10757	1166	90.2
Cooler	73.46	28.11	45.36	38.3
Gas turbine cycle				
Air compressor 1	751.9	676	75.89	89.9
Air compressor 2	718.1	642.2	33.72	89.4
Heat exchanger 1	104.8	54.08	50.76	51.6
Heat exchanger 2	8122	6737	1384	83.0
Gas turbine	4401	4235	148.4	96.6
Air preheater	1544	994.7	549.5	64.4
Kalina cycle				
Evaporator	1900	1676	224.4	88.2
Turbine	1456	1274	181.6	87.5
Recuperator 1	72.75	41.23	31.52	56.7
Recuperator 2	223.3	173.5	49.82	77.7
Condenser 1	96.22	29.65	66.57	30.8
Condenser 2	47.71	13.98	33.72	29.3
Pump 1	2.051	1.444	0.6072	70.4
Pump 2	35.1	24.78	10.32	70.6
Separator	27583	27576	7.563	99.9
Mixer 1	35116	35112	4.01	99.9
Mixer 2	17460	17452	8.104	99.9
Splitter	35028	35028	~0	100
Throttling valve	17734	17722	11.41	99.9
Supercritical CO_2 cycle				
Turbine	987.6	943.7	43.91	95.6
Main compressor	289.7	257.6	32.13	88.9
Re-compressor	190.9	175.3	15.61	91.8
High temperature recuperator	660.3	607.6	52.77	92.0
Low temperature recuperator	467.4	404.1	63.3	86.5
Generator	841.6	831.2	10.4	98.8
Mixer	2432	2432	0.054	100
Organic Rankine cycle				
Turbine	210.1	171.3	38.81	81.5
Evaporator	223.6	160.4	63.18	71.8
Pump	0.5375	0.4314	0.106	80.3
Condenser	13.93	12.2	1.724	87.6
Steam Rankine cycle				
Evaporator	1216	1159	57.77	95.3
Turbine	1118	957.1	160.7	85.6
Pump	4.826	3.908	0.9176	81.0
Condenser	102.6	35.16	67.47	34.3
Wastewater treatment unit				
Separator 1	429	352.9	76.19	82.2
Heat exchanger 4	9835	9707	127	98.7
Throttling valve	27.18	26.38	0.7952	97.1
Separator 2	301.5	282.8	18.67	93.8
Heat exchanger 5	9665	6030	3634	62.4
Mixer	9712	9665	47.3	99.5
PEME				
PEM electrolyzer	622.4	333.1	289.3	53.5
Carbon capture unit				
Compressor	1500	1271	228.8	84.8
Heat exchanger 3	1284	1003	281	78.1
Absorber column	1301	1144	157.8	87.9
Throttling valve	542.3	153.5	388.7	28.3
Separator	153.5	71.45	82.09	46.5
Methanation Unit				
Pump 3	2.001	1.84	0.1612	92.0
Heat exchanger 6	0.1736	0.1703	0.0033	98.1
Pump 4	2.089	1.881	0.2085	90.0
Heat exchanger 7	0.5483	0.4225	0.1258	77.1
Heat exchanger 8	0.2574	0.1602	0.09716	62.3
Mixer	187.4	187.4	0	100
Sabatier reactor	187.4	168.9	18.44	90.2

of 35.08 % and an exergy efficiency of 39.89 %, making it the most efficient scenario among the three. The dual production scenario offers a balanced approach with energy efficiency at 34.98 % and exergy efficiency at 39.86 %, allowing flexibility to meet demands for both fuels without significant efficiency trade-offs. These scenarios provide insights into optimizing synthetic fuel production based on market needs and efficiency considerations.

4.4. *Sensitivity analysis*

Although the system model comprises many variables, only a few strongly affect its performance. To identify these critical factors, all variables were systematically examined within specified ranges that reflect the system's technical limitations and are supported by relevant literature. The parameters found to be most impactful are illustrated in Figs. 8–14.

4.4.1. *PEME cell number*

Fig. 8 illustrates that increasing the number of PEM electrolyzer (PEME) cells results in higher hydrogen production, rising from 107 kg/day up to 161 kg/day at the maximum cell count. However, this increase comes with a marginal reduction in both energy and exergy efficiencies. The primary reason for this decrease is the notable rise in electrical power consumption by the PEME stack, which climbs from 508 kW to 768 kW as cells are added. This elevated power demand decreases the net power output of the overall system, which is a significant factor contributing to the slight dip in efficiency metrics.

4.4.2. *Kalina evaporator pinch-point temperature difference*

As Fig. 9 shows, increasing the pinch-point temperature difference, from 10 K to 40 K, leads to higher exergy destruction, causing a slight drop in exergy efficiency from 40.0 % to 39.5 %. Conversely, energy efficiency experiences a modest rise because it equally counts all energy forms and benefits from the increased district water heating capacity, which grows from 1200 kW to 1540 kW. Notably, the hydrogen production rate remains stable throughout these changes, indicating that the pinch-point temperature difference affects thermal performance more than fuel generation.

4.4.3. *Pressure ratio of air compressor 1*

Fig. 10 demonstrates that raising the pressure ratio of compressor 1 leads to a significant improvement in both energy efficiency, increasing from 33.0 % to 41.0 %, and exergy efficiency, rising from 38.0 % to 44.0 %. This enhancement is primarily driven by a notable increase in the district water heating capacity, which grows from 1200 kW to 1750 kW across the range, while the net power output remains largely constant. It is important to note that hydrogen production remains unaffected by changes in the compressor's pressure ratio, indicating this parameter mainly influences the thermal energy side of the system.

4.4.4. *Pressure ratio of air compressor 2*

Fig. 11 shows that increasing the pressure ratio in compressor 2 enhances both energy efficiency, rising from 33.7 % to 39.2 %, and exergy efficiency, increasing more substantially from 37.9 % to 46.6 %. This improvement primarily results from a significant gain in net power output, which rises from 3420 kW to 3740 kW, despite a slight reduction in district water heating capacity. Since hydrogen-related parameters remain largely unaffected by changes in this compressor's pressure ratio, the hydrogen production rate stays nearly constant.

4.4.5. *Main compressor pressure ratio*

Fig. 12 shows that increasing main compressor pressure ratio leads to higher power consumption by the component, but it simultaneously drives a significant gain in net power production from the ORC, supercritical CO_2, and thermoelectric generator units. As a result, the total net power output increases from 3185 kW to 3680 kW across the examined range. This improvement translates into enhanced system efficiencies, with energy efficiency rising from 32.7 % to 36.0 % and exergy efficiency improving from 36.7 % to 41.5 %. Despite these changes in power generation and efficiencies, the hydrogen production rate remains essentially unchanged.

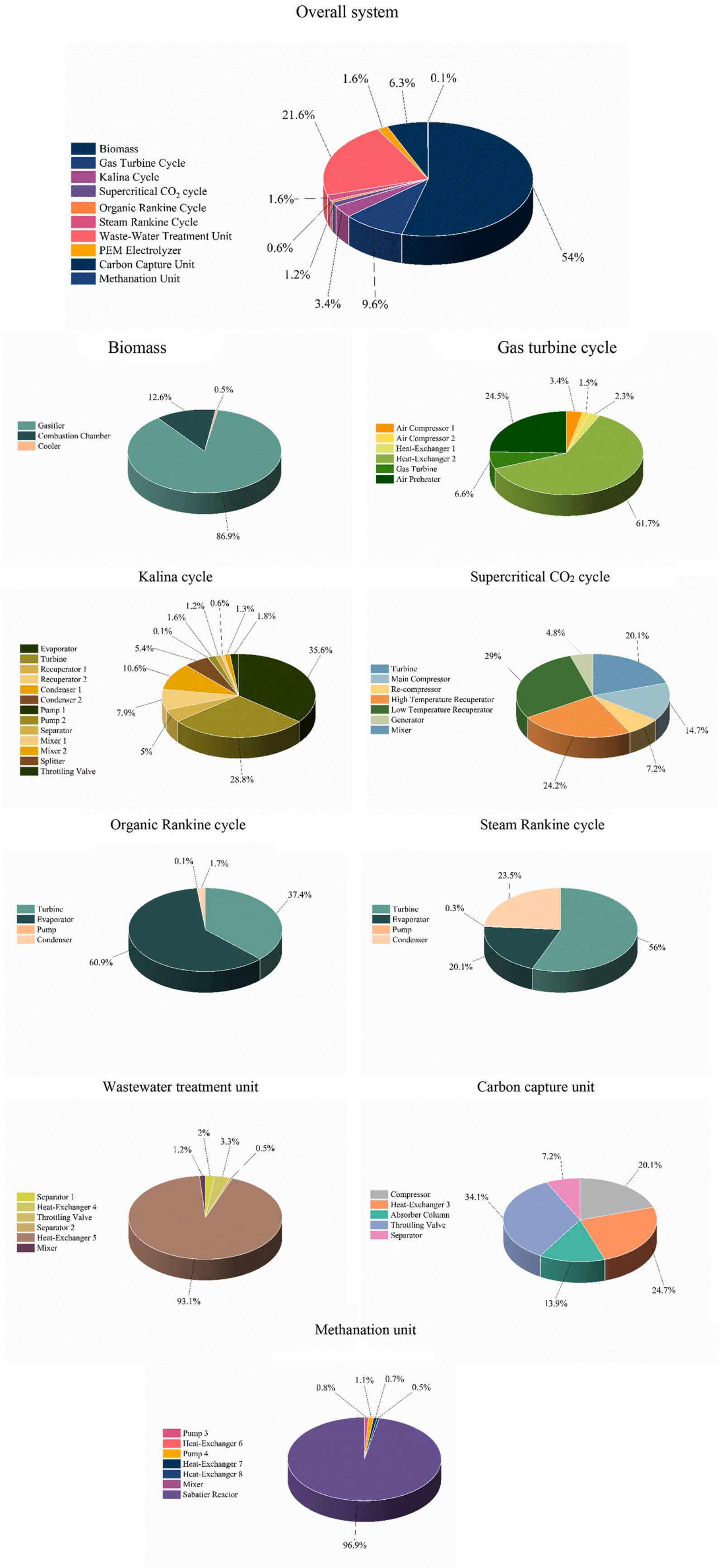

Fig. 6. Exergy destruction distribution across subsystems and components.

Table 11
Main performance indicators of proposed polygeneration system for baseline operation.

Performance criteria	Value
Energy efficiency (%)	35.0
Exergy efficiency (%)	39.9
Methane production rate (kg/day)	296.3
Hydrogen production rate (kg/day)	131.6
Oxygen production rate (kg/day)	2106
Heating load (kW)	1310
Captured CO_2 rate (t/day)	177.8
Treated water production rate (m^3/day)	116.6
Net power production rate (kW)	3510
Total exergy destruction rate (kW)	17800

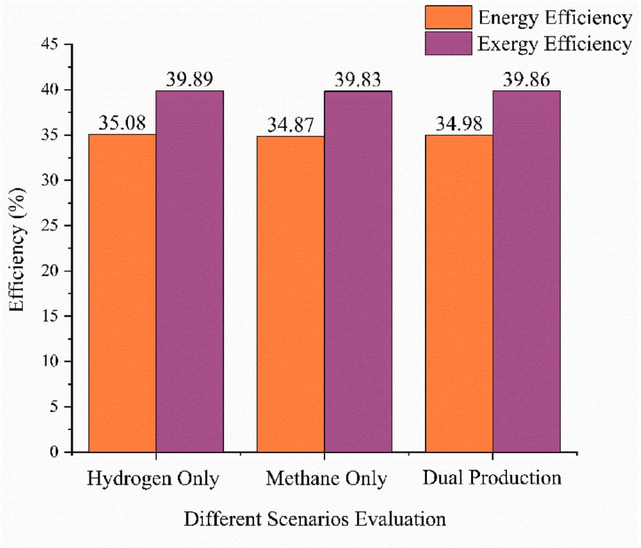

Fig. 7. Comparison of energy and exergy efficiencies for hydrogen-only, methane-only, and dual production scenarios in fuel production in baseline condition.

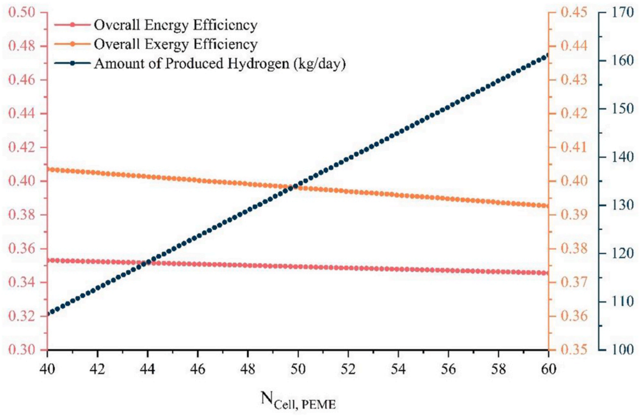

Fig. 8. Effect of PEME cell count on the optimization objective functions.

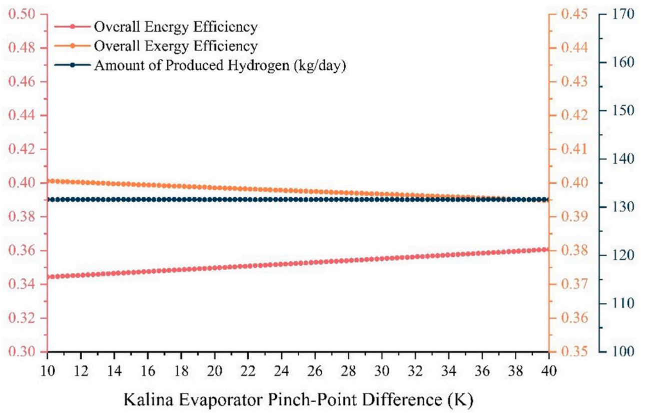

Fig. 9. Effect of Kalina evaporator pinch-point temperature difference on the optimization objective functions.

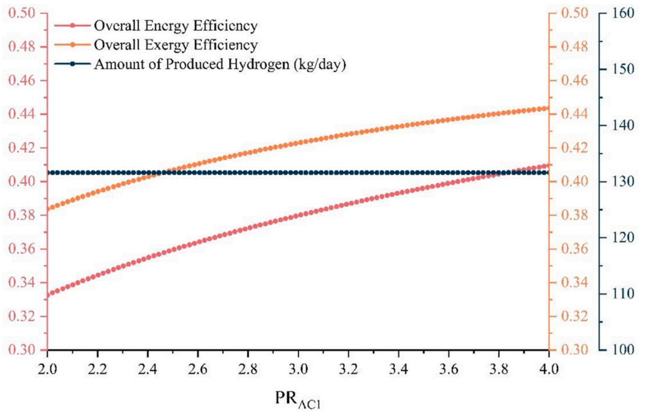

Fig. 10. Effect of the pressure ratio of air compressor 1 on the optimization objective functions.

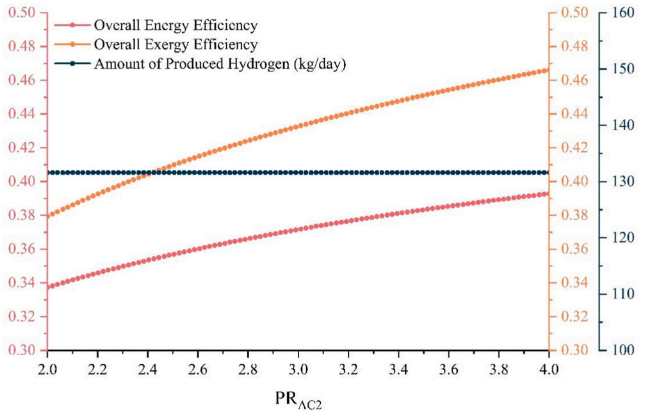

Fig. 11. Effect of the pressure ratio of air compressor 2 on the optimization objective functions.

4.4.6. Re-compressor pressure ratio

Fig. 13 illustrates that increasing the re-compressor pressure ratio from 2 to 4 results in a slight reduction in energy efficiency, decreasing from 35.5 % to 34.5 %, and a decrease in exergy efficiency from 40.6 % to 39.2 %. This decline is mainly due to the increased energy consumption of the compressor at higher pressure ratios, which reduces the net power output of the system. Importantly, this adjustment does not affect the energy, heat, or fuel production rates, and the hydrogen production rate remains stable with this variation.

4.4.7. Inlet temperature of gas turbine

As illustrated in Fig. 14, increasing the gas turbine inlet temperature from 1300 K to 1600 K results in declines in both energy and exergy efficiencies. This reduction mainly stems from a decrease in district water heating output rate, which falls from 1380 kW to 1280 kW, as well as a drop in net power output from 3640 kW to 3200 kW. Consequently,

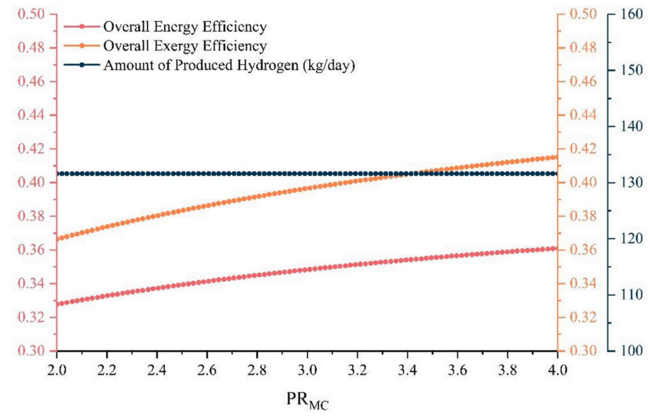

Fig. 12. Influence of the pressure ratio of the main compressor on the optimization objective functions.

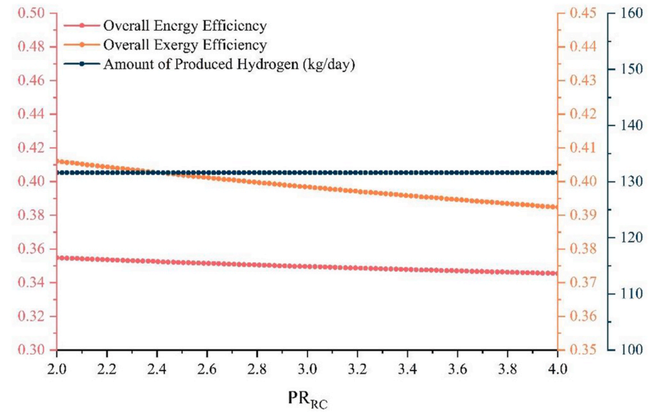

Fig. 13. Influence of the pressure ratio of the re-compressor on the optimization objective functions.

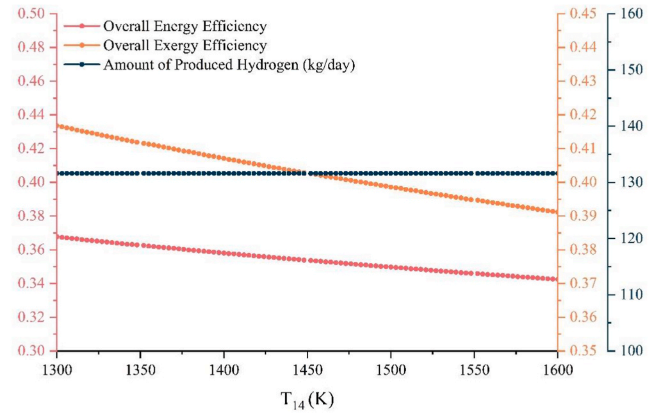

Fig. 14. Impact of gas turbine's inlet temperature (T_{14}) on the optimization objective functions.

energy efficiency declines from 36.7 % to 34.4 %, and exergy efficiency decreases from 41.6 % to 39.0 %. The hydrogen production rate remains largely unaffected across this temperature range.

4.5. *Multi-objective optimization*

The sensitivity analysis indicated that several design and operating parameters strongly affect the system's thermodynamic performance and hydrogen production capacity. To obtain a configuration that balances these trade-offs, a tri-objective optimization framework was developed. The optimization simultaneously targeted three conflicting objectives: maximizing energy efficiency, maximizing exergy efficiency, and maximizing the hydrogen production rate. The optimization procedure was implemented through a MATLAB-based framework utilizing artificial neural network (ANN) surrogate models. These highly accurate ANNs, with R^2 values exceeding 0.98 for all objectives, replaced computationally expensive direct simulations, enabling rapid evaluation of potential solutions. Four multi-objective metaheuristic algorithms, grey wolf optimizer (GWO), genetic algorithm (GA), non-dominated sorting genetic algorithm II (NSGA-II), and multi-objective particle swarm optimization (MOPSO), were employed to identify the best-performing approach for this problem. The linear multi-attribute decision process (LINMAP) method was subsequently applied to select the most suitable configuration from the final Pareto front. The following subsections present, first, a comparative evaluation of the applied algorithms and, second, the detailed results obtained using the selected GWO-based optimization.

4.5.1. *Comparative evaluation of optimization algorithms*

To identify the most effective optimization algorithm for the developed hydrogen production system, four well-known multi-objective techniques, GWO, GA, NSGA-II, and MOPSO, were implemented and tested under identical parameter settings, search ranges, and computational budgets within the MATLAB-based framework. All methods simultaneously optimized the three conflicting objectives: maximizing energy efficiency, maximizing exergy efficiency, and maximizing hydrogen production rate. The evaluation employed four established multi-objective performance indicators: normalized hypervolume (HV_n), inverted generational distance (IGD), epsilon (ε) indicator, and spread (Δ). All objective values were normalized to the [0, 1] range to ensure equitable comparison, and the non-dominated union of all obtained Pareto fronts served as the reference set for the IGD and ε calculations.

Table 12 summarizes the comparative results. GWO achieved the lowest IGD (0.0086) and ε (0.0739), indicating its solutions were closest to the reference Pareto front and demonstrated the strongest dominance performance among the tested algorithms. Although GA produced the highest hypervolume ($HV_n = 25.58$), it exhibited poor uniformity ($\Delta = 2.08$), suggesting an uneven and clustered distribution of solutions along the front. MOPSO provided the most uniform Pareto front ($\Delta = 0.80$) and a competitive ε indicator (0.0361) but showed slightly weaker convergence ($IGD = 0.0146$) compared with GWO. NSGA-II performed moderately in terms of diversity but recorded the highest IGD (0.0734), confirming slower convergence towards the optimal front.

Overall, GWO demonstrated the most balanced trade-off between convergence to the optimal set of solutions and diversity across the entire performance spectrum. This balance provided a reliable and comprehensive set of Pareto-optimal solutions for the hydrogen production system with minimal parameter tuning. Therefore, GWO was selected as the most suitable algorithm for the final tri-objective optimization of the proposed system. The resulting Pareto front from the GWO algorithm will then be used as the input for the LINMAP method to

Table 12
Performance comparison of multi-objective optimization algorithms.

Algorithm	HV_n	IGD	ε	Spread	Remarks
GWO	20.69	0.0086	0.0739	0.97	Closest to reference front; balanced and stable
GA	25.59	0.04563	0.2031	2.078	Highest converge but poor uniformity
NSGA-II	9.72	0.0734	0.1900	0.89	Moderate diversity, weakest convergence
MOPSO	15.27	0.0146	0.0361	0.79	Most uniform distribution, strong dominance

identify the final optimal operating point.

4.5.2. Optimization performance of the proposed system

Following the algorithm comparison, the Grey Wolf Optimizer was applied to identify the optimal design configuration for the polygeneration system. Fig. 15 illustrates the Pareto front obtained from MOGWO, with each point representing a potential optimal design. The LINMAP-selected solution, highlighted in the figure, represents the most balanced trade-off between the competing objectives.

The optimized system achieved significant performance enhancements across all key metrics. Energy and exergy efficiencies reached 49.5 % and 53.6 %, respectively, corresponding to improvements of 41.5 % and 34.4 % over the baseline configuration. Hydrogen and methane production increased by 23.0 %, while total exergy destruction decreased by 1.4 %, demonstrating that the optimization both enhanced output and reduced irreversibilities for more efficient resource use. Table 13 summarizes the comprehensive performance comparison between the optimized and baseline systems. Notably, while net power output decreased by 6.9 % due to the prioritization of fuel production, heating load and oxygen production increased substantially by 29.1 % and 23.0 %, respectively. Fig. 16 further illustrates the optimized system's performance under various fuel production scenarios, highlighting its flexibility and adaptability to different operational priorities.

A detailed comparison with related waste-to-energy and waste-to-x studies is provided in Table 14, where the proposed system is benchmarked against existing technologies in terms of feedstock types, products, subsystem configurations, performance indicators, and the presence or absence of carbon capture, wastewater treatment, and advanced optimization. Compared with previous works, the present system uniquely combines municipal solid waste and wastewater treatment with MEA-based CO_2 capture, CCU via methanation, and freshwater production, enabling near-zero-emission operation while co-producing electricity, heat, hydrogen, methane, and oxygen. Although some referenced systems achieve higher efficiencies for specific services, they typically lack integrated wastewater treatment, comprehensive carbon capture/utilization, or multi-vector fuel production, resulting in a narrower functional scope. In the proposed configuration, multiple thermodynamic cycles (S-CO_2, Kalina, ORC, and TEG) recover waste heat across a wide temperature range, increasing net power output and subsequently enhancing hydrogen production through PEM electrolysis, an energy interaction most comparable systems do not exploit. Environmentally, many studies in Table 14 omit CO_2 capture or consider only storage, whereas the combination of MEA-based capture with methanation in our system both reduces emissions and converts CO_2 into valuable fuel, strengthening its alignment with net-zero objectives. Moreover, consolidating carbon capture, wastewater treatment, and fuel production within a single platform avoids the need for separate units and reduces external energy demand, providing operational and economic advantages. Overall, the proposed concept delivers competitive energy (49.5 %) and exergy (53.6 %) efficiencies while offering broader environmental and functional benefits than existing alternatives, highlighting its potential as a versatile and sustainability-oriented waste-to-x option for urban applications.

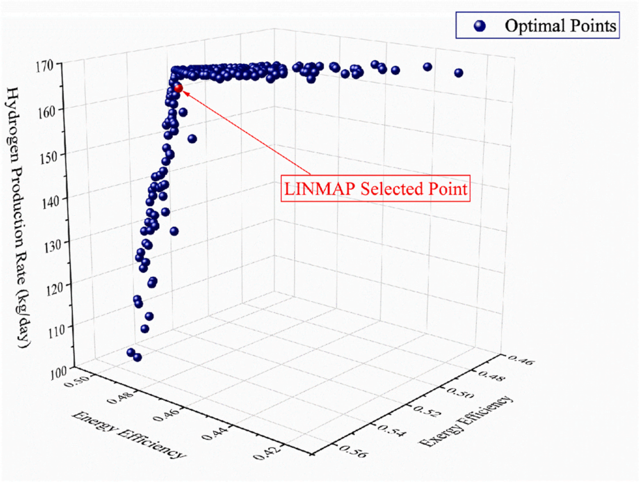

Fig. 15. Pareto-optimal solutions obtained from the multi-objective optimization.

Table 13
Comparison between baseline and optimized results for the proposed system.

Performance criteria	Baseline	Optimal point	Difference
Energy efficiency (%)	35.0	49.5	+41.5 %
Exergy efficiency (%)	39.9	53.6	+34.4 %
Methane production rate (kg/day)	296	364	+23.0 %
Hydrogen production rate (kg/day)	131.6	162	+23.0 %
Oxygen production rate (kg/day)	2106	2589	+23.0 %
Heating load (kW)	1310	1695	+29.1 %
Net power production rate (kW)	3510	3270	−6.9 %
Total exergy destruction rate (kW)	17800	17550	−1.4 %

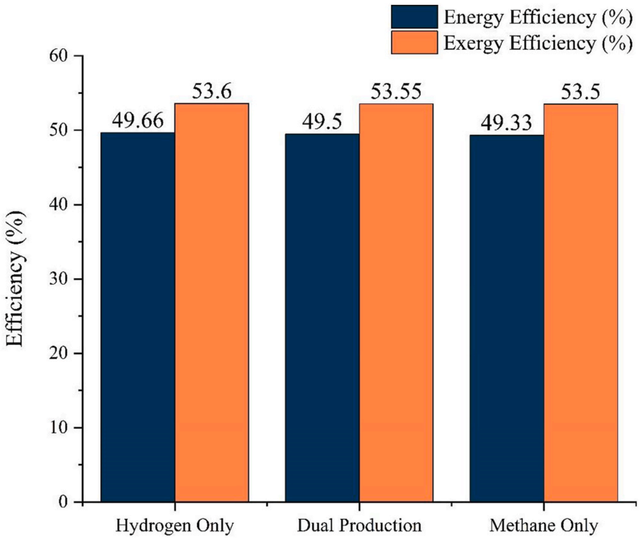

Fig. 16. Comparison of energy and exergy efficiencies for hydrogen-only, methane-only, and dual production scenarios in fuel production in optimal point.

4.6. Advantages, challenges, and implementation prospects of the proposed polygeneration framework

The comparative analysis in Table 14 underscores the innovative features and practical advantages of the proposed waste-to-x polygeneration system. Unlike many existing technologies, the proposed system uniquely integrates municipal solid waste and wastewater treatment with advanced carbon capture and utilization through methanation, alongside freshwater production, delivering a holistic option that enables near-zero-emission operation. This multi-fuel, multi-product approach distinguishes the system from typical configurations that often focus on single outputs or lack critical functions such as integrated wastewater treatment and comprehensive carbon capture. The adoption of a machine learning-based multi-objective optimization framework further enhances the system's adaptability and operational resilience, making it well-suited for dynamic feedstock compositions and variable urban operating conditions. The high energy and exergy efficiencies achieved demonstrate its potential as a scalable, versatile, and environmentally sustainable technology. From a practical

Table 14
Comparative assessment of system performance with earlier works.

Ref.	Municipal waste types	Productions	Subsystems	Analysis	Energy efficiency (%)	Exergy efficiency (%)	Power (kW)/ Heating (kW)/ Cooling (kW)/ Fuel production (kg/day)	Carbon capture and utilization
Present study	MSW Wastewater	Power Heating Hydrogen Methane	Gasification Gas turbine SCO_2 Kalina ORC SRC Carbon capture Wastewater treatment Methanation PEME TEG	Energy Exergy Sensitivity GW multi-objective optimization ML Multi-scenario	49.5	53.6	3270/ 1700/ -/ H_2 161.8/ CH_4 364.4	✓
Chen et al. [58] (2022)	MSW	Power	Gasification Incineration Gas turbine Steam turbine	Energy Exergy Economic	37.8	34.9	4240/ -/ -/ -/ -/	×
Hai et al. [59] (2023)	MSW	Power	Gasification Gas turbine Rankine Geothermal	Energy Exergy Parametric study environmental	–	47.6	8025/ -/ -/ -/ -/	×
Wang et al. [60] (2025)	MSW	Power Heating Cooling Hydrogen	Gasification Gas turbine SRC Single effect chiller PEME	Energy Exergy Economic Environmental GWO optimization	59.0	26.4	2484/ 3303/ 1166/ H_2 290.4/ -/	×
Tera et al. [61] (2024)	MSW	Power Heating Hydrogen	Gasification Reforming SOFC ORC S-CO_2	Energy Exergy Economic Emergy	76.8	60.6	5640/ 9260/ -/ H_2 15170/ -/	×
Eisavi et al. [62] (2024)	MSW	Power Methane Methanol	Gasification Rankine ORC Methanation PEME MCFC Methanol unit	Energy Exergy Exergoeconomic	41.8	36.8	7300/ -/ -/ CH_4 450/ Methanol 988/	✓
Khoshgoftar Manesh et al. [63] (2024)	MSW Wastewater	Power Freshwater	Gasification FPC ICE ORC HDH RO Wastewater treatment MDC Carbon storage	Energy Exergy Exergoeconomic Exergo-environmental Emergo-economic Sensitivity optimization	34.5	5.9	460/ -/ -/ -/ -/ H_2O 128.6 (m^3/day)	Carbon capture and storage

perspective, this system offers a viable option for urban centers seeking to enhance waste valorization, improve resource recovery, and meet stringent emission targets. Its integrated design facilitates seamless incorporation into existing urban infrastructure, addressing real-world challenges in waste management, energy production, and environmental compliance, thereby advancing sustainable urban development. The methodology in this study represents a green approach by applying Green Chemistry Principles such as waste prevention, use of renewable feedstocks, energy efficiency, process intensification, and integrated separation and recovery [64,65]. Regarding the integration of carbon capture and methanation, while innovative options at early development stages may not yet match the cost-effectiveness of mature technologies, their implementation remains essential for achieving net-zero emissions. High-pressure compressors used in carbon capture units can consume a substantial portion of the system's generated power, reducing efficiencies and increasing operational costs, particularly in MEA-based processes. Nevertheless, ongoing technological advancements are expected to enhance performance and reduce costs over time. Among the three main carbon capture methods discussed, post-combustion capture is the most mature and suitable for industrial-scale application [66]. Considering both the technical and economic challenges, along with scalability prospects, offers a balanced and realistic perspective on the system's practical implementation.

5. Conclusion

This research introduces and evaluates the design of an innovative waste-to-x polygeneration system that integrates multiple advanced technologies, including biomass gasification, a gas turbine cycle, supercritical CO_2 cycle, Kalina cycle, organic Rankine cycle, steam Rankine cycle, wastewater treatment unit, carbon capture unit, PEM electrolyzer, and a methanation unit. The proposed configuration allows for concurrent generation of electricity, heating, hydrogen, and methane, offering a holistic approach to sustainable energy utilization and waste valorization.

A thorough energy and exergy analysis was performed to evaluate the system's performance. To further enhance efficiency, the system parameters were optimized using a machine learning-based MOGWO algorithm. The design accommodates three distinct fuel production scenarios: hydrogen-only, methane-only, and dual-fuel (hydrogen and methane) production. The key findings of this study, and the conclusions drawn from them, follow:

- Under baseline conditions, the designed system exhibits an overall energy efficiency of 35.0 % and an exergy efficiency of 39.9 %.
- In the baseline condition, the system delivers a net power generation of 3510 kW, provides a heating load of 1310 kW, and produces hydrogen, oxygen, and methane at rates of 131 kg/day, 2106 kg/day, and 296 kg/day, respectively.
- The system achieves high environmental sustainability by capturing 87 % of CO_2 emissions (177.7 tons/day) and treating 116.6 tons/day of wastewater, significantly reducing emissions and promoting responsible waste and water management.
- Exergy analysis revealed that the biomass subsystem contributes the most to total exergy destruction, accounting for nearly 54.0 %, whereas the methanation unit exhibits the lowest contribution at only 0.1 %. Major sources of exergy destruction include the gasifier (8014 kW), heat exchanger 5 (3634 kW), and the combustion chamber (1166 kW). In contrast, components such as pumps, splitters, and mixers exhibit minimal exergy destruction. Notably, mixers and splitters demonstrate the highest exergy efficiencies, exceeding 99.0 %, while the lowest exergy efficiencies are observed in the throttling valve of the carbon capture unit (28.3 %), condenser 2 (29.3 %), condenser 1 (30.8 %), and the steam Rankine cycle condenser (34.3 %).
- Optimization resulted in significant improvements in system performance, increasing energy efficiency from 35.0 % to 49.5 % and exergy efficiency from 39.9 % to 53.6 %. Hydrogen production also increased by 23.0 %.
- Additional performance enhancements in the optimized system include reductions of 6.9 % in net power output and 1.4 % in overall rate of exergy degradation, along with increases of 23.0 % in methane and oxygen production rates and 29.1 % in heating load.
- In the optimal condition, among the fuel production scenarios, the hydrogen-only scenario achieves the highest energy and exergy efficiencies at 49.7 % and 53.6 %, respectively, whereas the methane-only scenario yields the lowest values at 49.3 % and 53.5 %, respectively.

These findings confirm the practicality of a scalable, efficient, and environmentally sustainable multi-generation of electricity, heat, hydrogen, methane, and oxygen through the proposed eco-friendly polygeneration framework. The system's competitive advantage lies in its integration of diverse waste sources, such as municipal solid waste and wastewater, with advanced machine learning-based optimization techniques. The outcomes of this research contribute meaningful perspectives for the advancement of waste management technologies and the promotion of a cleaner, more resilient, and sustainable energy transition.

Overall, the results demonstrate the technical feasibility of a scalable and environmentally sustainable multi-generation system for electricity, heat, hydrogen, methane, and oxygen based on integrated urban waste streams. However, this work is limited to thermodynamic performance assessment and optimization; more detailed analyses, including techno-economic evaluations, life cycle environmental assessments, and policy or market feasibility studies, are important next steps. In practical urban applications, the proposed concept requires further evaluation regarding capital and operating costs, infrastructure and space requirements, feedstock availability and quality, regulatory constraints, and integration with existing waste and energy networks. Future research should focus on quantifying these economic and environmental indicators, exploring various scales and deployment scenarios, and addressing social and economic challenges such as community acceptance and job creation. Additionally, emerging questions about the scalability of such systems, their long-term operational sustainability, and the potential for integration with renewable energy sources should be explored to enhance the broader relevance of this research.

CRediT authorship contribution statement

Mohammadreza Babaei Khuyinrud: Writing – original draft, Visualization, Validation, Software, Methodology, Data curation, Conceptualization. **Ali Shokri Kalan:** Writing – original draft, Visualization, Validation, Supervision, Software, Methodology, Formal analysis, Conceptualization. **Borhan Pourtalebi:** Writing – original draft, Validation, Software, Methodology, Data curation. **Mehran Ahamdi:** Writing – original draft, Validation, Software, Methodology. **Iraj Jangi:** Writing – original draft, Validation, Software, Methodology. **Xiaoshu Lü:** Writing – review & editing, Supervision, Methodology, Conceptualization. **Yanping Yuan:** Writing – review & editing, Methodology, Conceptualization. **Marc A. Rosen:** Writing – review & editing, Supervision, Methodology, Data curation, Conceptualization.

Declaration of competing interest

The authors declare that they have no known competing financial interests or personal relationships that could have appeared to influence the work reported in this paper.

Acknowledgement

The authors acknowledge the financial support provided by the CETPartnership (OptiDCG4H2, Grant No. CETP-2023-00567).

Appendix A. Supplementary data

Supplementary data to this article can be found online at https://doi.org/10.1016/j.energy.2026.140052.

Data availability

Data will be made available on request.

References

[1] Naghipour P, Naghipour A. Energy performance analysis of residential buildings in Bandar Anzali: influence of orientation and aspect ratio. Sustainability 2025;5: 100140. https://doi.org/10.1016/j.nxsust.2025.100140.

[2] Naghipour P, Naghipour A, Shirdel A, Behzadi S, Rahaei O, Salamati S. Sustainability in historical Islamic architecture: lessons from Sheikh Lotfollah Mosque's construction techniques. J Islamic Arch Jun. 2025;8(3):585–603. https://doi.org/10.18860/jia.v8i3.29053.

[3] Bioenergy International. European Biomethane Map shows 37% increase in EU RNG capacity. Bioenergy International; 2024. https://bioenergyinternational.com/2024-european-biomethane-map-shows-37-increase-in-eu-rng-capacity. [Accessed 28 September 2025].

[4] Gholizadeh T, Abbaspour N, Ghiasirad H, Skorek-Osikowska A. Sustainable biofuel production through anaerobic digestion, SOEC and carbon-capture-and-utilization (CCU): techno-economic, exergy and life-cycle analysis. Energy Aug. 2025;328: 136458. https://doi.org/10.1016/j.energy.2025.136458.

[5] Peng W, Chen H, Liu J, Zhao X, Xu G. Techno-economic assessment of a conceptual waste-to-energy CHP system combining plasma gasification, SOFC, gas turbine and supercritical CO_2 cycle. Energy Convers Manag Oct. 2021;245:114622. https://doi.org/10.1016/j.enconman.2021.114622.

[6] Saravanan A, Yaashikaa PR, Senthil Kumar P, Vickram AS, Karishma S, Kamalesh R, Rangasamy G. Techno-economic and environmental sustainability prospects on biochemical conversion of agricultural and algal biomass to biofuels. https://doi.org/10.1016/j.jclepro.2023.137749; Aug. 2023.

[7] Skorek-Osikowska A. Thermodynamic and environmental study on synthetic natural gas production in power to gas approaches involving biomass gasification

and anaerobic digestion. Int J Hydrogen Energy Jan. 2022;47(5):3284–93. https://doi.org/10.1016/j.ijhydene.2021.01.002.

[8] Bellver-Domingo Á, Hernández-Sancho F. Circular economy and payment for ecosystem services: a framework proposal based on water reuse. J Environ Manag Mar. 2022;305:114416. https://doi.org/10.1016/j.jenvman.2021.114416.

[9] Omidi Kashani B, Khoshbakhti Saray R, Kheiri R. Comparative analysis of a CCHP system based on municipal solid waste (MSW) gasification using micro gas turbine and internal combustion engine: energy, exergy, economic, and environmental (4E) perspectives. Energy Jul. 2025;326:136004. https://doi.org/10.1016/j.energy.2025.136004.

[10] Lee J, Lin K-YA, Jung S, Kwon EE. Hybrid renewable energy systems involving thermochemical conversion process for waste-to-energy strategy. Chem Eng J Jan. 2023;452:139218. https://doi.org/10.1016/j.cej.2022.139218.

[11] Han J, Byun J, Kwon O, Lee J. Climate variability and food waste treatment: analysis for bioenergy sustainability. Renew Sustain Energy Rev May 2022;160: 112336. https://doi.org/10.1016/j.rser.2022.112336.

[12] Fegade SL. Green hydrocarbons and fuels from municipal polymer waste co-fed with natural gas using a batch catalytic slurry process. Green Technol Sustain Sep. 2024;2(3):100099. https://doi.org/10.1016/j.grets.2024.100099.

[13] Wang W, Zhao Q, Lu B, Shi J, Jin H. Pure hydrogen gas production in a coal supercritical water gasification system with CO_2 as transporting medium. Appl Therm Eng Sep. 2023;237:121529. https://doi.org/10.1016/j.applthermaleng.2023.121529.

[14] Tezer Ö, Karabağ N, Öngen A, Çolpan CÖ, Ayol A. Biomass gasification for sustainable energy production: a review. Int J Hydrogen Energy Apr. 2022;47(34): 15419–33. https://doi.org/10.1016/j.ijhydene.2022.02.158.

[15] Lu X, Du B, Zhu W, Yang Y, Xie C, Tu Z, Zhao B, Zhang L, Song J, Deng Z. Thermodynamic and dynamic analysis of a hybrid PEMFC-ORC combined heat and power (CHP) system. Energy Convers Manag Jul. 2023;292:117408. https://doi.org/10.1016/j.enconman.2023.117408.

[16] Liu X, Hu G, Zeng Z. Potential of biomass processing using digester in arrangement with a Brayton cycle, a Kalina cycle, and a multi-effect desalination; thermodynamic/environmental/financial study and MOPSO-based optimization. Energy Dec. 2022;261:125222. https://doi.org/10.1016/j.energy.2022.125222.

[17] Biancini G, Cioccolanti L, Moradi R, Moglie M. Comparative study of steam, organic Rankine cycle and supercritical CO_2 power plants integrated with residual municipal solid waste gasification for district heating and cooling. Appl Therm Eng Jan. 2024;241:122437. https://doi.org/10.1016/j.applthermaleng.2024.122437.

[18] Rokni M. Thermodynamic analyses of municipal solid waste gasification plant integrated with solid oxide fuel cell and Stirling hybrid system. Int J Hydrogen Energy Jun. 2015;40(24):7855–69. https://doi.org/10.1016/j.ijhydene.2014.11.046.

[19] Soltani MM, Ahmadi P, Ashjaee M. Techno-economic optimization of a biomass gasification energy system with Supercritical CO_2 cycle for hydrogen fuel and electricity production. Fuel Feb. 2023;333:126264. https://doi.org/10.1016/j.fuel.2022.126264.

[20] Du J, Zou Y, Dahlak A. Process development and multi-criteria optimization of a biomass gasification unit combined with a novel CCHP model using helium gas turbine, kalina cycles, and dual-loop organic flash cycle. Energy Mar. 2024;291: 130319. https://doi.org/10.1016/j.energy.2024.130319.

[21] Naghipour P, Naghipour A. Evaluating heating energy consumption in residential buildings using hybrid machine learning models: the case of parsabad city. Research Sep. 2025;2(3):100721. https://doi.org/10.1016/j.nexres.2025.100721.

[22] Agarwal A. Computational investigation of vertical axis wind turbine in hydrogen gas generation using PEM electrolysis. J N Mater Electrochem Syst Aug. 2022;25 (3):172–8. https://doi.org/10.14447/jnmes.v25i3.a03.

[23] Kalan AS, Heidarabadi S, Khaleghi M, Ghiasirad H, Skorek-Osikowska A. Biomass-to-energy integrated trigeneration system using supercritical CO_2 and modified Kalina cycles: energy and exergy analysis. Energy Feb. 2023;270:126845. https://doi.org/10.1016/j.energy.2023.126845.

[24] Xiao Z, Wu W. Environmental sustainability by an integrated system based on municipal solid waste fluidized bed gasification using energy, exergy, and environmental analyses. Appl Therm Eng Dec. 2023;239:122171. https://doi.org/10.1016/j.applthermaleng.2023.122171.

[25] Biancini G, Cioccolanti L, Chen H, Kyprianidis K, Dahlquist E, Moglie M. Integration of multiple energy systems for the valorisation of the residual municipal solid waste: a modelling study. Energy Mar. 2025;318:134813. https://doi.org/10.1016/j.energy.2025.134813.

[26] Kemper J. Biomass and carbon dioxide capture and storage: a review. Int J Greenh Gas Control Sep. 2015;40:401–30. https://doi.org/10.1016/j.ijggc.2015.06.012.

[27] Theo WL, Lim JS, Hashim H, Mustaffa AA, Ho WS. Review of pre-combustion capture and ionic liquid in carbon capture and storage. Appl Energy Dec. 2016; 183:1633–63. https://doi.org/10.1016/j.apenergy.2016.09.103.

[28] Guo P, Xue Q, Wang J, Bai P, Gu M, Hua J, Duan P. The exploration of the essential need for decarbonization and the achievement of zero energy consumption in the CHP + carbon capture system. Energy Jan. 2025. https://doi.org/10.1016/j.energy.2025.134534. 134534–134534.

[29] Rezaei S, Liu A, Hovington P. Emerging technologies in post-combustion carbon dioxide capture & removal. Catal Today Nov. 2023;423:114286. https://doi.org/10.1016/j.cattod.2023.114286.

[30] Krótki A, Więcław-Solny L, Tatarczuk A, Spietz T, Chwoła T, Dobras S. A pilot study comparing MEA and AEEA solvents in carbon capture. Int J Greenh Gas Control Jun. 2023;126:103891. https://doi.org/10.1016/j.ijggc.2023.103891.

[31] Dong B, Wang S, Thorin E, Sun Q, Li H. Negative emission potential from biomass/waste combined heat and power plants integrated with CO_2 capture: an approach from the national perspective. J Clean Prod Jun. 2024;467:142917. https://doi.org/10.1016/j.jclepro.2024.142917.

[32] Zhu Y, Zhang C, Yan M, Liu Z, Li W, Li H, Wang Y. Biomass-fired combined heat, cool and power system incorporating organic Rankine cycle and single-effect lithium bromide absorption refrigeration integrated with CO_2 capture: thermo-economic analysis. Energy Jun. 2024;304:132096. https://doi.org/10.1016/j.energy.2024.132096.

[33] Beiron J, Normann F, Johnsson F. A techno-economic assessment of CO_2 capture in biomass and waste-fired combined heat and power plants – a Swedish case study. Int J Greenh Gas Control Jul. 2022;118:103684. https://doi.org/10.1016/j.ijggc.2022.103684.

[34] Rabiee A, Keane A, Soroudi A. Green hydrogen: a new flexibility source for security constrained scheduling of power systems with renewable energies. Int J Hydrogen Energy May 2021;46(37):19270–84. https://doi.org/10.1016/j.ijhydene.2021.03.080.

[35] Ratib MK, Muttaqi KM, Islam MR, Sutanto D, Agalgaonkar AP. Electrical circuit modeling of proton exchange membrane electrolyzer: the state-of-the-art, current challenges, and recommendations. Int J Hydrogen Energy Jan. 2024;49:625–45. https://doi.org/10.1016/j.ijhydene.2023.08.319.

[36] Mekonnin AS, Wacławiak K, Humayun M, Zhang S, Ullah H. Hydrogen storage technology, and its challenges: a review. Catalysts Mar. 2025;15(3):260. https://doi.org/10.3390/catal15030260.

[37] McLaughlin H, Littlefield AA, Menefee M, Kinzer A, Hull T, Sovacool BK, Bazilian MD, Kim J, Griffiths S. Carbon capture utilization and storage in review: sociotechnical implications for a carbon reliant world. Renew Sustain Energy Rev May 2023;177:113215. https://doi.org/10.1016/j.rser.2023.113215.

[38] Li W, Wang H, Jiang X, Zhu J, Liu Z, Guo X, Song C. A short review of recent advances in CO_2 hydrogenation to hydrocarbons over heterogeneous catalysts. RSC Adv Feb. 2018;8(14):7651–69. https://doi.org/10.1039/C7RA13546G.

[39] Tommasi M, Degerli SN, Ramis G, Rossetti I. Advancements in CO_2 methanation: a comprehensive review of catalysis, reactor design and process optimization. Chem Eng Res Des Jan. 2024;201:457–82. https://doi.org/10.1016/j.cherd.2023.11.060.

[40] Jalili M, Holagh SG, Chitsaz A, Song J, Markides CN. Electrolyzer cell-methanation/Sabatier reactors integration for power-to-gas energy storage: thermo-economic analysis and multi-objective optimization. Appl Energy Jan. 2023;329:120268. https://doi.org/10.1016/j.apenergy.2022.120268.

[41] Sabbaghi M, Baniasadi E, Genceli H. Thermodynamic assessment of an innovative biomass-driven system for generating power, heat, and hydrogen. Int J Hydrogen Energy Mar. 2024. https://doi.org/10.1016/j.ijhydene.2024.03.196.

[42] García-Luna S, Ortiz C. Partial oxycombustion and amines-driven waste-to-methane for improved Carbon Capture and Utilization (CCU). Energy Convers Manag Jan. 2024;302:118125. https://doi.org/10.1016/j.enconman.2024.118125.

[43] Schyllander J, Sandberg M, Venkatesh G. Modeling, energy analysis, and greenhouse gas-footprint analysis of a proposed industrial symbiotic system including algal cultivation, a combined heat and power plant and a wastewater treatment plant. Biofuels Bioenergy 2025:271–97. https://doi.org/10.1016/b978-0-443-29254-5.00012-6.

[44] Gupta AS, Khatiwada D. Investigating the sustainability of biogas recovery systems in wastewater treatment plants- A circular bioeconomy approach. Renew Sustain Energy Rev Jul. 2024;199:114447. https://doi.org/10.1016/j.rser.2024.114447.

[45] Khuyinrud MB, Kalan AS, Ghiasirad H, Gholizadeh T, Lü X, Arabkoohsar A. A novel biomass-to-energy cogeneration system using zeotropic mixtures: multi-objective optimization and environmental assessment. Process Saf Environ Prot Mar. 2025: 106976. https://doi.org/10.1016/j.psep.2025.106976.

[46] laleh SS, Gharamaleki FP, Fatemi Alavi S, Soltani S, Mahmoudi SMS, Rosen MA. A novel sustainable biomass-fueled cogeneration cycle integrated with carbon dioxide capture utilizing LNG regasification and green hydrogen production via PEM electrolysis: thermodynamic assessment. J Clean Prod Oct. 2023;421:138529. https://doi.org/10.1016/j.jclepro.2023.138529.

[47] Khuyinrud MB, Fallah M, Seyed M, Ehghaghi MB. Technoeconomic and advanced exergy analysis of a molten-salt-driven Kalina cycle under full-load and part-load conditions: a machine learning-based multi-objective optimization. Energy Convers Manag Sep. 2025;X:101300. https://doi.org/10.1016/j.ecmx.2025.101300.

[48] Aziz F, Salim MS, Kim M-H. Performance analysis of high temperature cascade organic Rankine cycle coupled with water heating system. Energy Mar. 2019;170: 954–66. https://doi.org/10.1016/j.energy.2018.12.210.

[49] Nazari N, Porkhial S. Multi-objective optimization and exergo-economic assessment of a solar-biomass multi-generation system based on externally-fired gas turbine, steam and organic Rankine cycle, absorption chiller and multi-effect desalination. Appl Therm Eng Oct. 2020;179:115521. https://doi.org/10.1016/j.applthermaleng.2020.115521.

[50] Kalan AS, Khuyinrud MB, Jahangiri F, Ahmadi R, Mahboubi A, Lü X, Rosen MA. Thermodynamic analysis and performance enhancement of an integrated solar–geothermal polygeneration system using grey wolf optimization and LSTM-based forecasting with Monte Carlo uncertainty analysis: a case study on Tenerife Island. Appl Energy Aug. 2025;401:126640. https://doi.org/10.1016/j.apenergy.2025.126640.

[51] Eisavi B, Ranjbar F, Nami H, Chitsaz A. Low-carbon biomass-fueled integrated system for power, methane and methanol production. Energy Convers Manag Feb. 2022;253:115163. https://doi.org/10.1016/j.enconman.2021.115163.

[52] ErikØi L. Comparison of aspen HYSYS and aspen plus simulation of CO_2 absorption into MEA from atmospheric gas. Energy Proc 2012;23:360–9. https://doi.org/10.1016/j.egypro.2012.06.036.

[53] Sardroud RG, Khuyinrud MB, Nami H. Advanced exergy and exergoeconomic analyses and multi-objective optimization of geothermal-driven organic flash cycles. Renew Energy Feb. 2025:122630. https://doi.org/10.1016/j.renene.2025.122630.

[54] Rostami S, Ghiasirad H, Rostamzadeh H, Kalan AS, Maleki A. A wind turbine driven hybrid HDH-MED-MVC desalination system towards minimal liquid discharge. South Afr J Chem Eng Apr. 2023;44:356–69. https://doi.org/10.1016/j.sajce.2023.03.007.

[55] Kalan AS, Ghiasirad H, Saray RK, Mirmasoumi S. Thermo-economic evaluation and multi-objective optimization of a waste heat driven combined cooling and power system based on a modified Kalina cycle. Energy Convers Manag Nov. 2021;247: 114723. https://doi.org/10.1016/j.enconman.2021.114723.

[56] Jarungthammachote S, Dutta A. Thermodynamic equilibrium model and second law analysis of a downdraft waste gasifier. Energy Sep. 2007;32(9):1660–9. https://doi.org/10.1016/j.energy.2007.01.010.

[57] Ohya H, Fun J, Kawamura H, Itoh K, Ohashi H, Aihara M, Tanisho S, Negishi Y. Methanation of carbon dioxide by using membrane reactor integrated with water vapor permselective membrane and its analysis. J Membr Sci Aug. 1997;131(1–2): 237–47. https://doi.org/10.1016/s0376-7388(97)00055-0.

[58] Chen H, Li J, Li T, Xu G, Jin X, Wang M, Liu T. Performance assessment of a novel medical-waste-to-energy design based on plasma gasification and integrated with a municipal solid waste incineration plant. Energy Apr. 2022;245:123156. https://doi.org/10.1016/j.energy.2022.123156.

[59] Hai T, Zhou J, Almashhadani YS, Chaturvedi R, Alshahri AH, Almujibah HR, Sayed Mohammed Metwally A, Ullah M. Thermo-economic and environmental assessment of a combined cycle fueled by MSW and geothermal hybrid energies. Process Saf Environ Prot May 2023;176:260–70. https://doi.org/10.1016/j.psep.2023.05.067.

[60] Wang F, Wang L, Sadeq AM, Alsenani TR, Muhammad T. Biomass gasification combined with a novel heat integration design for sustainable energy supply programs: comprehensive thermodynamic, environmental, and economic evaluations. Energy Sep. 2025:138560. https://doi.org/10.1016/j.energy.2025.138560.

[61] Tera I, Zhang S, Liu G. A conceptual hydrogen, heat and power polygeneration system based on biomass gasification, SOFC and waste heat recovery units: energy, exergy, economic and emergy (4E) assessment. Energy May 2024;295:131015. https://doi.org/10.1016/j.energy.2024.131015.

[62] Eisavi B, Nami H, Ranjbar F, Sharifi A. Economic assessment and optimization of low-carbon biomass-based power, methane, and methanol production. Int J Hydrogen Energy Jan. 2024;52:869–88. https://doi.org/10.1016/j.ijhydene.2023.11.025.

[63] Khoshgoftar Manesh M, Davadgaran S, Rabeti S. Novel solar-biomass polygeneration system based on integration of ICE-ORC-MDC-HDH-RO and tomato greenhouse to produce power, freshwater, and biological wastewater treatment. Energy Convers Manag Apr. 2024;308:118349. https://doi.org/10.1016/j.enconman.2024.118349.

[64] Fegade SL. Red chemistry: principles and applications. Sustainability 2024;4: 100048. https://doi.org/10.1016/j.nxsust.2024.100048.

[65] Fegade SL. Assessment of greenness of catalytic deoxygenation of crop oil for green diesel production. Clean Circ Bioecon Aug. 2024;8:100091. https://doi.org/10.1016/j.clcb.2024.100091.

[66] Vinjarapu S, Løge I, Neerup R, Larsen A, Rasmussen V, Jørsboe J, Villadsen Sebastian N, Jensen S, Karlsson J, Kappel J, Lassen H, Blinksbjerg P, Solms N, Fosbøl P. Learnings from up-scaling CO_2 capture: challenges and experiences with pilot work. Chem Eng Sci Aug. 2024;300. https://doi.org/10.1016/j.ces.2024.120576. 120576–120576.

Update

Energy

Volume 346, Issue , 1 March 2026, Page

DOI: https://doi.org/10.1016/j.energy.2026.140354

Energy 346 (2026) 140354

Contents lists available at ScienceDirect

Energy

journal homepage: www.elsevier.com/locate/energy

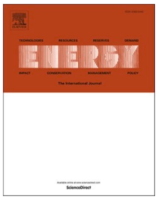

Corrigendum

Corrigendum to “Design, performance assessment, and machine learning-driven optimization of a novel low-carbon urban waste-to-x polygeneration system: multi-scenario analysis of hydrogen and methane production” [Energy (2026) Article 140052]

Mohammadreza Babaei Khuyinrud [a], Ali Shokri Kalan [b,*], Borhan Pourtalebi [c], Mehran Ahmadi [d], Iraj Jangi [e], Xiaoshu Lü [b,f], Yanping Yuan [g], Marc A. Rosen [h]

[a] *Faculty of Mechanical Engineering, Sahand University of Technology, P.O. Box 51335-1996, Sahand New Town, Tabriz, Iran*
[b] *Renewable Energy and Built Environment, University of Vaasa, P.O. Box 700, FIN-65101, Vaasa, Finland*
[c] *Chemical Engineering Faculty, Sahand University of Technology, P.O. Box 51335-1996, Sahand New Town, Tabriz, Iran*
[d] *Department of Industrial Engineering, University of Padova, Via Venezia 1, 35131, Padova, Italy*
[e] *Faculty of Chemical and Petroleum Engineering, University of Tabriz, 29 Bahman Blvd., Tabriz, Iran*
[f] *Department of Civil Engineering, Aalto University, P.O. Box. 11000, FIN-02130, Finland*
[g] *School of Mechanical Engineering, Southwest Jiaotong University, Chengdu, 610031, China*
[h] *Faculty of Engineering and Applied Science, University of Ontario Institute of Technology, Oshawa, Ontario, L1G 0C5, Canada*

The authors regret that an author's name and affiliation were published with typographical errors. The author name “Mehran Ahamdi” should read “Mehran Ahmadi.” In addition, in affiliation (d), the city name was incorrectly written as “Pado-va” and should read “Padova.” These corrections do not affect the scientific content or conclusions of the article.The authors would like to apologise for any inconvenience caused.

DOI of original article: https://doi.org/10.1016/j.energy.2026.140052.

* Corresponding author.
E-mail address: Ali.shokrikalan@uwasa.fi (A.S. Kalan).

https://doi.org/10.1016/j.energy.2026.140354